

Dijet photoproduction at HERA and the structure of the photon

ZEUS Collaboration

Abstract

The dijet cross section in photoproduction has been measured with the ZEUS detector at HERA using an integrated luminosity of 38.6 pb^{-1} . The events were required to have a virtuality of the incoming photon, Q^2 , of less than 1 GeV^2 and a photon-proton centre-of-mass energy in the range $134 < W_{\gamma p} < 277 \text{ GeV}$. Each event contains at least two jets satisfying transverse-energy requirements of $E_T^{\text{jet}1} > 14 \text{ GeV}$ and $E_T^{\text{jet}2} > 11 \text{ GeV}$ and pseudorapidity requirements of $-1 < \eta^{\text{jet}1,2} < 2.4$. The measurements are compared to next-to-leading-order QCD predictions. The data show particular sensitivity to the density of partons in the photon, allowing the validity of the current parameterisations to be tested.

The ZEUS Collaboration

S. Chekanov, M. Derrick, D. Krakauer, S. Magill, B. Musgrave, A. Pellegrino, J. Repond,
R. Yoshida

Argonne National Laboratory, Argonne, Illinois 60439-4815ⁿ

M.C.K. Mattingly

Andrews University, Berrien Springs, Michigan 49104-0380

P. Antonioli, G. Bari, M. Basile, L. Bellagamba, D. Boscherini, A. Bruni, G. Bruni,
G. Cara Romeo, L. Cifarelli, F. Cindolo, A. Contin, M. Corradi, S. De Pasquale, P. Giusti,
G. Iacobucci, G. Levi, A. Margotti, T. Massam, R. Nania, F. Palmonari, A. Pesci, G. Sar-
torelli, A. Zichichi

University and INFN Bologna, Bologna, Italy^e

G. Aghuzumtsyan, D. Bartsch, I. Brock, J. Crittenden¹, S. Goers, H. Hartmann, E. Hilger,
P. Irrgang, H.-P. Jakob, A. Kappes, U.F. Katz², R. Kerger, O. Kind, E. Paul, J. Rautenberg³,
R. Renner, H. Schnurbusch, A. Stifutkin, J. Tandler, K.C. Voss, A. Weber, H. Wessoleck
Physikalisches Institut der Universität Bonn, Bonn, Germany^b

D.S. Bailey⁴, N.H. Brook⁴, J.E. Cole, B. Foster, G.P. Heath, H.F. Heath, S. Robins,
E. Rodrigues⁵, J. Scott, R.J. Tapper, M. Wing

H.H. Wills Physics Laboratory, University of Bristol, Bristol, United Kingdom^m

M. Capua, A. Mastroberardino, M. Schioppa, G. Susinno

Calabria University, Physics Department and INFN, Cosenza, Italy^e

H.Y. Jeoung, J.Y. Kim, J.H. Lee, I.T. Lim, K.J. Ma, M.Y. Pac⁶

Chonnam National University, Kwangju, Korea^g

A. Caldwell, M. Helbich, X. Liu, B. Mellado, S. Paganis, W.B. Schmidke, F. Sciulli
Nevis Laboratories, Columbia University, Irvington on Hudson, New York 10027^o

J. Chwastowski, A. Eskreys, J. Figiel, K. Olkiewicz, M.B. Przybycień⁷, P. Stopa, L. Za-
wiejski

Institute of Nuclear Physics, Cracow, Polandⁱ

B. Bednarek, I. Grabowska-Bold, K. Jeleń, D. Kisielewska, A.M. Kowal⁸, M. Kowal,
T. Kowalski, B. Mindur, M. Przybycień, E. Rulikowska-Zarebska, L. Suszycki, D. Szuba,
J. Szuba⁹

*Faculty of Physics and Nuclear Techniques, University of Mining and Metallurgy, Cracow,
Polandⁱ*

A. Kotański, W. Słomiński¹⁰

Department of Physics, Jagellonian University, Cracow, Poland

L.A.T. Bauerdick¹¹, U. Behrens, K. Borras, V. Chiochia, D. Dannheim, K. Desler¹², G. Drews, J. Fourletova, A. Fox-Murphy, U. Fricke, A. Geiser, F. Goebel, P. Göttlicher, R. Graciani, T. Haas, W. Hain, G.F. Hartner, S. Hillert, U. Kötz, H. Kowalski, H. Labes, D. Lelas, B. Löhr, R. Mankel, J. Martens¹³, M. Martínez¹¹, M. Moritz, D. Notz, M.C. Petrucci, A. Polini, U. Schneekloth, F. Selonke, S. Stonjek, B. Surrow¹⁴, J.J. Whitmore¹⁵, R. Wichmann¹⁶, G. Wolf, C. Youngman, W. Zeuner

Deutsches Elektronen-Synchrotron DESY, Hamburg, Germany

C. Coldewey¹⁷, A. Lopez-Duran Viani, A. Meyer, S. Schlenstedt
DESY Zeuthen, Zeuthen, Germany

G. Barbagli, E. Gallo, C. Genta, P. G. Pelfer
University and INFN, Florence, Italy^e

A. Bamberger, A. Benen, N. Coppola, P. Markun, H. Raach, S. Wölfe
Fakultät für Physik der Universität Freiburg i.Br., Freiburg i.Br., Germany^b

M. Bell, P.J. Bussey, A.T. Doyle, C. Glasman, S. Hanlon, S.W. Lee, A. Lupi, G.J. McCance, D.H. Saxon, I.O. Skillicorn
Department of Physics and Astronomy, University of Glasgow, Glasgow, United Kingdom^m

B. Bodmann, U. Holm, H. Salehi, K. Wick, A. Ziegler, Ar. Ziegler
Hamburg University, I. Institute of Exp. Physics, Hamburg, Germany^b

T. Carli, I. Gialas¹⁸, K. Klimek, E. Lohrmann, M. Milite
Hamburg University, II. Institute of Exp. Physics, Hamburg, Germany^b

C. Collins-Tooth, C. Foudas, R. Gonçalo⁵, K.R. Long, F. Metlica, D.B. Miller, A.D. Tapper, R. Walker
Imperial College London, High Energy Nuclear Physics Group, London, United Kingdom^m

P. Cloth, D. Filges
Forschungszentrum Jülich, Institut für Kernphysik, Jülich, Germany

M. Kuze, K. Nagano, K. Tokushuku¹⁹, S. Yamada, Y. Yamazaki
Institute of Particle and Nuclear Studies, KEK, Tsukuba, Japan^f

A.N. Barakbaev, E.G. Boos, N.S. Pokrovskiy, B.O. Zhautykov
Institute of Physics and Technology of Ministry of Education and Science of Kazakhstan, Almaty, Kazakhstan

S.H. Ahn, S.B. Lee, S.K. Park
Korea University, Seoul, Korea^g

H. Lim, D. Son

Kyungpook National University, Taegu, Korea^g

F. Barreiro, G. García, O. González, L. Labarga, J. del Peso, I. Redondo²⁰, J. Terrón,
M. Vázquez

Departamento de Física Teórica, Universidad Autónoma Madrid, Madrid, Spain^l

M. Barbi, A. Bertolin, F. Corriveau, A. Ochs, S. Padhi, D.G. Stairs, M. St-Laurent
Department of Physics, McGill University, Montréal, Québec, Canada H3A 2T8^a

T. Tsurugai

Meiji Gakuin University, Faculty of General Education, Yokohama, Japan

A. Antonov, V. Bashkirov²¹, P. Danilov, B.A. Dolgoshein, D. Gladkov, V. Sosnovtsev,
S. Suchkov

Moscow Engineering Physics Institute, Moscow, Russia^j

R.K. Dementiev, P.F. Ermolov, Yu.A. Golubkov, I.I. Katkov, L.A. Khein, N.A. Korotkova,
I.A. Korzhavina, V.A. Kuzmin, B.B. Levchenko, O.Yu. Lukina, A.S. Proskuryakov, L.M. Shche-
glova, A.N. Solomin, N.N. Vlasov, S.A. Zotkin

Moscow State University, Institute of Nuclear Physics, Moscow, Russia^k

C. Bokel, J. Engelen, S. Grijpink, E. Koffeman, P. Kooijman, E. Maddox, S. Schagen,
E. Tassi, H. Tiecke, N. Tuning, J.J. Velthuis, L. Wiggers, E. de Wolf

NIKHEF and University of Amsterdam, Amsterdam, Netherlands^h

N. Brümmner, B. Bylsma, L.S. Durkin, J. Gilmore, C.M. Ginsburg, C.L. Kim, T.Y. Ling
*Physics Department, Ohio State University, Columbus, Ohio 43210*ⁿ

S. Boogert, A.M. Cooper-Sarkar, R.C.E. Devenish, J. Ferrando, T. Matsushita, M. Rigby,
O. Ruske²², M.R. Sutton, R. Walczak

Department of Physics, University of Oxford, Oxford United Kingdom^m

R. Brugnera, R. Carlin, F. Dal Corso, S. Dusini, A. Garfagnini, S. Limentani, A. Longhin,
A. Parenti, M. Posocco, L. Stanco, M. Turcato

Dipartimento di Fisica dell'Università and INFN, Padova, Italy^e

L. Adamczyk²³, B.Y. Oh, P.R.B. Saull²³

*Department of Physics, Pennsylvania State University, University Park, Pennsylvania
16802*^o

Y. Iga

Polytechnic University, Sagamihara, Japan^f

G. D'Agostini, G. Marini, A. Nigro

Dipartimento di Fisica, Università 'La Sapienza' and INFN, Rome, Italy^e

C. Cormack, J.C. Hart, N.A. McCubbin
Rutherford Appleton Laboratory, Chilton, Didcot, Oxon, United Kingdom^m

C. Heusch
*University of California, Santa Cruz, California 95064*ⁿ

I.H. Park
Seoul National University, Seoul, Korea

N. Pavel
Fachbereich Physik der Universität-Gesamthochschule Siegen, Germany

H. Abramowicz, S. Dagan, A. Gabareen, S. Kananov, A. Kreisel, A. Levy
Raymond and Beverly Sackler Faculty of Exact Sciences, School of Physics, Tel-Aviv University, Tel-Aviv, Israel^d

T. Abe, T. Fusayasu, T. Kohno, K. Umemori, T. Yamashita
Department of Physics, University of Tokyo, Tokyo, Japan^f

R. Hamatsu, T. Hirose, M. Inuzuka, S. Kitamura²⁴, K. Matsuzawa, T. Nishimura
Tokyo Metropolitan University, Department of Physics, Tokyo, Japan^f

M. Arneodo²⁵, N. Cartiglia, R. Cirio, M. Costa, M.I. Ferrero, S. Maselli, V. Monaco, C. Peroni, M. Ruspa, R. Sacchi, A. Solano, A. Staiano
Università di Torino, Dipartimento di Fisica Sperimentale and INFN, Torino, Italy^e

R. Galea, T. Koop, G.M. Levman, J.F. Martin, A. Mirea, A. Sabetfakhri
Department of Physics, University of Toronto, Toronto, Ontario, Canada M5S 1A7^a

J.M. Butterworth, C. Gwenlan, R. Hall-Wilton, M.E. Hayes²⁶, E.A. Heaphy, T.W. Jones, J.B. Lane, M.S. Lightwood, B.J. West
Physics and Astronomy Department, University College London, London, United Kingdom^m

J. Ciborowski²⁷, R. Ciesielski, G. Grzelak, R.J. Nowak, J.M. Pawlak, B. Smalska²⁸, J. Sztuk²⁹, T. Tymieniecka³⁰, A. Ukleja³⁰, J. Ukleja, J.A. Zakrzewski, A.F. Żarnecki
*Warsaw University, Institute of Experimental Physics, Warsaw, Poland*ⁱ

M. Adamus, P. Plucinski
*Institute for Nuclear Studies, Warsaw, Poland*ⁱ

Y. Eisenberg, L.K. Gladilin³¹, D. Hochman, U. Karshon
Department of Particle Physics, Weizmann Institute, Rehovot, Israel^c

J. Breitweg³², D. Chapin, R. Cross, D. Kçira, S. Lammers, D.D. Reeder, A.A. Savin, W.H. Smith
*Department of Physics, University of Wisconsin, Madison, Wisconsin 53706*ⁿ

A. Deshpande, S. Dhawan, V.W. Hughes, P.B. Straub
Department of Physics, Yale University, New Haven, Connecticut 06520-8121 ⁿ

S. Bhadra, C.D. Catterall, S. Fourletov, S. Menary, M. Soares, J. Standage
Department of Physics, York University, Ontario, Canada M3J 1P3 ^a

- ¹ now at Cornell University, Ithaca/NY, USA
- ² on leave of absence at University of Erlangen-Nürnberg, Germany
- ³ supported by the GIF, contract I-523-13.7/97
- ⁴ PPARC Advanced fellow
- ⁵ supported by the Portuguese Foundation for Science and Technology (FCT)
- ⁶ now at Dongshin University, Naju, Korea
- ⁷ now at Northwestern Univ., Evanston/IL, USA
- ⁸ supported by the Polish State Committee for Scientific Research, grant no. 5 P-03B 13720
- ⁹ partly supported by the Israel Science Foundation and the Israel Ministry of Science
- ¹⁰ Department of Computer Science, Jagellonian University, Cracow
- ¹¹ now at Fermilab, Batavia/IL, USA
- ¹² now at DESY group MPY
- ¹³ now at Philips Semiconductors Hamburg, Germany
- ¹⁴ now at Brookhaven National Lab., Upton/NY, USA
- ¹⁵ on leave from Penn State University, USA
- ¹⁶ now at Mobilcom AG, Rendsburg-Büdelndorf, Germany
- ¹⁷ now at GFN Training GmbH, Hamburg
- ¹⁸ Univ. of the Aegean, Greece
- ¹⁹ also at University of Tokyo
- ²⁰ supported by the Comunidad Autonoma de Madrid
- ²¹ now at Loma Linda University, Loma Linda, CA, USA
- ²² now at IBM Global Services, Frankfurt/Main, Germany
- ²³ partly supported by Tel Aviv University
- ²⁴ present address: Tokyo Metropolitan University of Health Sciences, Tokyo 116-8551, Japan
- ²⁵ also at Università del Piemonte Orientale, Novara, Italy
- ²⁶ now at CERN, Geneva, Switzerland
- ²⁷ also at Łódź University, Poland
- ²⁸ supported by the Polish State Committee for Scientific Research, grant no. 2 P-03B 00219
- ²⁹ Łódź University, Poland
- ³⁰ sup. by Pol. State Com. for Scien. Res., 5 P-03B 09820 and by Germ. Fed. Min. for Edu. and Research (BMBF), POL 01/043
- ³¹ on leave from MSU, partly supported by University of Wisconsin via the U.S.-Israel BSF
- ³² now at EssNet Deutschland GmbH, Hamburg, Germany

- ^a supported by the Natural Sciences and Engineering Research Council of Canada (NSERC)
- ^b supported by the German Federal Ministry for Education and Research (BMBF), under contract numbers HZ1GUA 2, HZ1GUB 0, HZ1PDA 5, HZ1VFA 5
- ^c supported by the MINERVA Gesellschaft für Forschung GmbH, the Israel Science Foundation, the U.S.-Israel Binational Science Foundation, the Israel Ministry of Science and the Benozvio Center for High Energy Physics
- ^d supported by the German-Israeli Foundation, the Israel Science Foundation, and by the Israel Ministry of Science
- ^e supported by the Italian National Institute for Nuclear Physics (INFN)
- ^f supported by the Japanese Ministry of Education, Science and Culture (the Monbusho) and its grants for Scientific Research
- ^g supported by the Korean Ministry of Education and Korea Science and Engineering Foundation
- ^h supported by the Netherlands Foundation for Research on Matter (FOM)
- ⁱ supported by the Polish State Committee for Scientific Research, grant no. 115/E-343/SPUB-M/DESY/P-03/DZ 121/2001-2002
- ^j partially supported by the German Federal Ministry for Education and Research (BMBF)
- ^k supported by the Fund for Fundamental Research of Russian Ministry for Science and Education and by the German Federal Ministry for Education and Research (BMBF)
- ^l supported by the Spanish Ministry of Education and Science through funds provided by CICYT
- ^m supported by the Particle Physics and Astronomy Research Council, UK
- ⁿ supported by the US Department of Energy
- ^o supported by the US National Science Foundation

1 Introduction

In photoproduction at HERA, a quasi-real photon, emitted from the incoming positron, collides with a parton from the incoming proton. The photoproduction of jets can be classified into two types of process in leading-order (LO) Quantum Chromodynamics (QCD). In direct processes (Fig. 1(a)), the photon participates in the hard scatter via either boson-gluon fusion or QCD Compton scattering. The second class, resolved processes (Fig. 1(b)), involve the photon acting as a source of quarks and gluons, with only a fraction of its momentum participating in the hard scatter. Measurements of jet cross sections in photoproduction [1–8] are thus sensitive to the structure of the photon and the proton, and to the dynamics of the hard sub-processes as calculated in perturbative QCD (pQCD). These jet cross sections can therefore be used in global fits to data to determine the parton densities in both the photon and proton.

In the kinematic range of the measurements presented in this paper, the value of x_p , the fractional momentum at which partons inside the proton are probed, lies predominantly in the region between 0.01 and 0.1. At these x_p values, the parton densities in the proton are constrained by measurements of the structure function, F_2^p , [9] in deep inelastic scattering (DIS). The present measurements are directly sensitive to both the quark and the gluon content of the photon. The fractional momentum of the photon carried by the interacting parton, x_γ , lies between 0.1 and 1. For x_γ values above 0.5, the quark densities in the photon are not well constrained by F_2^γ data obtained from $\gamma\gamma^*$ scattering in e^+e^- experiments [10–16]. The gluon density, to which jet photoproduction is directly sensitive at LO, is also poorly constrained by the F_2^γ data for all x_γ . The most recent measurements of F_2^γ from LEP extend up to an average scale of ~ 25 GeV. These, and higher scales, can be studied in jet production at HERA.

The aim of the present investigation is to provide constraints, from data on dijet photoproduction, on the parton densities in the photon in the range $0.1 < x_\gamma < 1$ and to probe the dynamics of the hard sub-processes. For this purpose, the dijet cross section is measured at high transverse energies where next-to-leading-order (NLO) QCD calculations are expected to describe the data. In this kinematic region, where the effects of soft physics are suppressed and the parton densities in the proton are well known, the data can be used to test the validity of the current parameterisations of the parton densities in the photon. At high x_γ , where the effects of the uncertainties in the photon structure are small, these data also provide a consistency check of the gluon distribution in the proton extracted from deep inelastic scattering.

This analysis builds on the improved understanding of jet photoproduction and of comparisons to NLO QCD calculations gained in previous analyses [2, 4]. With an increase of a factor of six in luminosity, an extension of the kinematic region and reduced systematic

uncertainties, the measurements in this paper¹ have greatly improved precision compared to the previous ZEUS dijet measurement [2].

2 Theoretical framework

Within the framework of pQCD, the dijet photon-proton cross section, $d\sigma_{\gamma p}$, can be written as a convolution of the proton parton density functions (PDFs), f_p , and photon PDFs, f_γ , with the partonic hard cross section, $d\hat{\sigma}_{ab}$:

$$d\sigma_{\gamma p} = \sum_{ab} \int_{x_p} \int_{x_\gamma} dx_p dx_\gamma f_p(x_p, \mu^2) f_\gamma(x_\gamma, \mu^2) d\hat{\sigma}_{ab}(x_p, x_\gamma, \mu^2) \cdot (1 + \delta_{\text{had}}).$$

For photoproduction cross sections measured in lepton-proton scattering, there is an additional convolution with the distribution of photons from the lepton beam. In the case of the direct cross section, the photon structure is replaced by a delta function at $x_\gamma = 1$. The scale of the process, μ , represents both the renormalisation scale, μ_R , and factorisation scale, μ_F , which are set equal for this study. The hadronisation correction, δ_{had} , accounts for non-perturbative effects in the final state and can be estimated using Monte Carlo (MC) models for the parton cascade and fragmentation; it is, in general, a function of the variable being measured (see Section 5).

The distribution of the dijet angle, θ^* , in the parton-parton centre-of-mass frame is directly sensitive to the form of the matrix elements, and hence to the partonic hard cross section. For massless partons, the centre-of-mass scattering angle is given by

$$\cos \theta^* = \tanh \left(\frac{\eta^{\text{jet1}} - \eta^{\text{jet2}}}{2} \right),$$

where η^{jet1} and η^{jet2} are the pseudorapidities in the laboratory frame of the two jets of highest transverse energy. Only the absolute value of $\cos \theta^*$ can be determined because the originating parton cannot be identified. The variable $\cos \theta^*$ is invariant under the different boosts along the beam axis arising from the spectrum of incoming parton momenta. This minimises the sensitivity of the differential cross section, $d\sigma/d\cos \theta^*$, to the momentum density distribution of the partons in the photon and proton.

¹ After submission of this paper, a similar study from the H1 collaboration became available [17].

For jets of transverse energy of more than 6 GeV, it has been shown [5] that samples of events enriched in either direct or resolved photon processes have very different angular distributions. The cross section for the sample enriched in resolved photon events increases more rapidly at high $\cos\theta^*$ than that in direct photon events. This is expected at both LO and NLO QCD [18]; both predictions give a good description of the data. The different angular dependence of the cross sections can be explained in terms of the dominant propagators in the respective samples. In direct events, the dominant processes (mostly boson-gluon fusion) have a spin- $\frac{1}{2}$ quark propagator and the angular dependence is approximately $\propto (1 - |\cos\theta^*|)^{-1}$. In resolved events (e.g. $qg \rightarrow qg$ and $gg \rightarrow gg$), the dominant processes have a spin-1 gluon propagator, which has an angular dependence $\propto (1 - |\cos\theta^*|)^{-2}$.

To probe the structure of the photon, it is desirable to measure cross sections as functions of variables that are sensitive to the spectrum of incoming parton momenta, such as the pseudorapidity of the jets or the momentum fraction, x_γ . Since x_γ is not directly measurable, an observable, x_γ^{obs} , which is the fraction of the photon's momentum participating in the production of the two highest transverse-energy jets (and is equal to x_γ for partons in LO QCD), is introduced [6]:

$$x_\gamma^{\text{obs}} = \frac{E_T^{\text{jet1}} e^{-\eta^{\text{jet1}}} + E_T^{\text{jet2}} e^{-\eta^{\text{jet2}}}}{2yE_e}.$$

Here E_T^{jet1} and E_T^{jet2} are the transverse energies of the two jets in the laboratory frame ($E_T^{\text{jet1}} > E_T^{\text{jet2}}$) and y is the fraction of the positron's energy, E_e , carried by the photon in the proton rest frame. The quantity x_γ^{obs} is a particularly useful variable with which to discriminate between various photon PDFs.

3 Experimental conditions

The data were collected during the 1996 and 1997 running periods, when HERA operated with protons of energy $E_p = 820$ GeV and positrons of energy $E_e = 27.5$ GeV, and correspond to an integrated luminosity of 38.6 ± 0.6 pb $^{-1}$. A detailed description of the ZEUS detector can be found elsewhere [19, 20]. A brief outline of the components that are most relevant for this analysis is given below.

The high-resolution uranium-scintillator calorimeter (CAL) [21] consists of three parts: the forward, the barrel and the rear calorimeters. Each part is subdivided transversely into towers and longitudinally into one electromagnetic and either one (in the rear) or two

(in the barrel and forward) hadronic sections. The smallest subdivision of the calorimeter is called a cell. The CAL relative energy resolutions, as measured under test-beam conditions, are $0.18/\sqrt{E}$ for electrons and $0.35/\sqrt{E}$ for hadrons (E in GeV).

Charged particles are measured in the central tracking detector (CTD) [22], which operates in a magnetic field of 1.43 T provided by a thin superconducting coil. The CTD covers the polar-angle² region $15^\circ < \theta < 164^\circ$. The relative transverse-momentum resolution for full-length tracks is $\sigma_{p_T}/p_T = 0.0058p_T \oplus 0.0065 \oplus 0.0014/p_T$ with p_T in GeV. Tracking information along with energy deposits in the CAL were used to measure the transverse energy and direction of jets as described in detail in Section 7.

The luminosity was measured from the rate of the bremsstrahlung process $e^+p \rightarrow e^+\gamma p$, where the photon was measured in a lead-scintillator calorimeter [23] placed in the HERA tunnel at $Z = -107$ m.

A three-level trigger system was used to select events online [4, 20]. At the third level, a cone algorithm was applied to the CAL cells and jets were reconstructed using the energies and positions of these cells. Events with at least two jets, each of which satisfied the requirements that the transverse energy exceeded 4 GeV and the pseudorapidity was less than 2.5, were accepted.

4 Definition of the cross section

The kinematic region for this study is the photoproduction region, defined as $Q^2 < 1\text{GeV}^2$, with a photon-proton centre-of-mass energy, $W_{\gamma p}$, in the range 134 GeV to 277 GeV. Each event is required to have at least two jets reconstructed with the k_T cluster algorithm [24] in its longitudinally invariant inclusive mode [25], with at least one jet having transverse energy greater than 14 GeV and another greater than 11 GeV. The jets are required to satisfy $-1 < \eta^{\text{jet}1,2} < 2.4$, an extension of the pseudorapidity range by 0.4 units in the forward direction over the previous analysis [2], thereby increasing the sensitivity of the measurement to resolved photon processes.

Cross sections are presented as a function of x_γ^{obs} , $E_T^{\text{jet}1}$ and $\eta^{\text{jet}2}$. The cross sections for jet variables are symmetrised [26] with respect to the pseudorapidities of the two jets. Each event, therefore, contributes twice to the cross section. The cross sections have been

² The ZEUS coordinate system is a right-handed Cartesian system, with the Z axis pointing in the proton beam direction, referred to as the “forward direction”, and the X axis pointing left towards the centre of HERA. The coordinate origin is at the nominal interaction point. The pseudorapidity is defined as $\eta = -\ln(\tan \frac{\theta}{2})$, where the polar angle, θ , is measured with respect to the proton beam direction.

determined for regions enriched in direct and resolved photon processes by requiring x_γ^{obs} to be greater than 0.75 or less than 0.75, respectively.

Additional kinematic constraints were applied to the measurement of the cross section as a function of $|\cos\theta^*|$ to remove biases imposed by the other requirements. For a given centre-of-mass energy, events at high $|\cos\theta^*|$ have small scattering angles and thus lower E_T^{jet} . To study the $|\cos\theta^*|$ distribution up to $|\cos\theta^*| = 0.8$ without bias from the E_T^{jet} requirements, a cut on the dijet mass of $M^{\text{jj}} > 42$ GeV was applied. The dijet mass is defined in terms of the two jets with highest transverse energy as

$$M^{\text{jj}} = \sqrt{2E_T^{\text{jet1}}E_T^{\text{jet2}} [\cosh(\eta^{\text{jet1}} - \eta^{\text{jet2}}) - \cos(\phi^{\text{jet2}} - \phi^{\text{jet1}})]},$$

where ϕ_1^{jet} and ϕ_2^{jet} are the azimuthal angles of the two jets. For jets back-to-back in azimuthal angle and of equal transverse energy, E_T^{jet} , the dijet mass is related to the scattering angle by

$$M^{\text{jj}} = \frac{2E_T^{\text{jet}}}{\sqrt{1 - |\cos\theta^*|^2}}. \quad (1)$$

When the minimum E_T^{jet} is taken to be 12.5 GeV, the average of the minimum transverse energies of the two jets, the requirement on the minimum dijet mass up to a given value of the scattering angle can be deduced from Eq. (1). Simulation studies show that the choice of cut dictated by this approximation does indeed eliminate any bias from the choice of transverse-energy cuts [27]. A further cut on the boost of the dijet system in the laboratory frame, $\bar{\eta} = (\eta^{\text{jet1}} + \eta^{\text{jet2}})/2$, of $0.1 < \bar{\eta} < 1.3$ was also applied. This ensures that the phase space is uniform as a function of $|\cos\theta^*|$, so that any shape seen in the measured distributions is attributable to the dynamics and not biased by the cuts imposed.

5 Monte Carlo models

The acceptance and the effects of detector response were determined using samples of simulated events. The programs HERWIG 6.1 [28] and PYTHIA 6.1 [29], which implement the leading-order matrix elements, followed by parton showers and hadronisation, were used. The HERWIG and PYTHIA generators differ in the details of the implementation of the leading-logarithmic parton-shower models. They also use different hadronisation models: HERWIG uses the cluster [30] model and PYTHIA uses the Lund string [31] model.

Direct and resolved events were generated separately. For all generated events, the ZEUS detector response was simulated in detail using a program based on GEANT 3.13 [32].

Parameters tuned to HERA data [33] were used in the generation of the HERWIG sample. The GRV-LO [34] and CTEQ4L [35] set of PDFs were used for the photon and proton, respectively. For the PYTHIA generator, the parameters were chosen to be consistent with fits to jet data from both HERA and LEP [36]. Here, the SaS-2D [37] and GRV94-LO [38] set of PDFs were used for the photon and proton, respectively. Multiparton interactions (MPI) were also included with a minimum transverse momentum of the secondary scatter of 2.0 GeV [39]. However, at the high transverse energies studied here, the effects of the “underlying event” are small: models with or without MPI describe the data equally well.

6 NLO QCD calculations

Many calculations of jet photoproduction at NLO exist [40–46], all of which have been compared with each other and agree to within (5 – 10)% [46, 47]. The calculation used here is that of Frixione and Ridolfi [40, 41], which employs the subtraction method [48] for dealing with the collinear and infra-red divergences. The number of flavours was set to 5 and the renormalisation and factorisation scales, μ , were set to half the sum of the transverse energies of the final-state partons, $E_T/2$. Two different parameterisations of the photon parton density were used³: GRV-HO [34] and AFG-HO [51]. The parton densities in the proton were parameterised using CTEQ5M1 [35]; the value $\alpha_s(M_Z) = 0.118$ used therein was adopted for the central prediction. The parameterisation MRST99 ($\alpha_s(M_Z) = 0.1175$) was also considered. Parameter settings in the NLO calculation were varied to test the stability of the theoretical predictions, as discussed in Section 10.

The NLO QCD predictions were corrected for hadronisation effects using a bin-by-bin procedure according to $d\sigma = d\sigma^{\text{NLO}} \cdot C_{\text{had}}^{-1}$, where $d\sigma^{\text{NLO}}$ is the cross section for partons in the final state of the NLO calculation. The hadronisation correction factor, $C_{\text{had}} \equiv (1 + \delta_{\text{had}})^{-1}$, was defined as the ratio of the dijet cross sections before and after the hadronisation process, $C_{\text{had}} = d\sigma_{\text{MC}}^{\text{partons}} / d\sigma_{\text{MC}}^{\text{hadrons}}$. The value of C_{had} was taken as the mean of the ratios obtained using the HERWIG and PYTHIA predictions. The hadronisation correction, δ_{had} , was generally below 10% in each bin except at the edges of phase space (see Tables 1–6). There are significant migrations in x_γ^{obs} for $x_\gamma^{\text{obs}} > 0.7$; however, the migrations to lower values are small.

³ The GS96-HO [49] parameterisation was not used because it has been shown that the available code does not reproduce the published results [50].

7 Energy corrections

Kinematic variables and jets were reconstructed using a combination of track and calorimeter information that optimises the resolution of reconstructed kinematic variables [52]. The selected tracks and calorimeter clusters are referred to as Energy Flow Objects (EFOs).

The addition of track information to the CAL information reduces the sensitivity to energy losses in inactive material in front of the CAL, and exploits the good momentum and angular resolution of the tracking for low-momentum particles. The energies of particles for which no track information was available (e.g. neutral particles), or for which the calorimeter energy resolution was better than that of the tracking (e.g. at the highest energies), were measured using CAL information. These energies were corrected for losses in the inactive material as discussed in a previous publication [2]. Conservation of energy and momentum in neutral current (NC) DIS events was exploited to determine the required energy corrections [53] by balancing the scattered positron with the hadronic final state. This was performed independently for data and simulated event samples. The EFOs thus corrected were used both to reconstruct jets and to determine kinematic variables. Comparisons of kinematic variables for data and simulated events led to the assignment of a 1% correlated systematic uncertainty in the transverse jet energies and in the hadronic variables [53]. The improved precision in this uncertainty compared with the previous measurement [2] was obtained from an increased data sample, better selection requirements and improved parameterisations of the energy losses. In the overlapping kinematic region, the total cross section measured here is 6% lower than the previous measurement [2], but within the quoted uncertainties arising from the uncertainty in the jet energy scale.

8 Event selection

After applying the energy corrections described in Section 7, dijet events were selected offline by using the following procedures and cuts designed to remove sources of background:

- the k_T clustering algorithm was applied to the corrected EFOs. Events were selected in which at least two jets were found with $-1 < \eta^{\text{jet}1,2} < 2.4$, $E_T^{\text{jet}1} > 14$ GeV and $E_T^{\text{jet}2} > 11$ GeV;
- to remove background due to proton beam-gas interactions and cosmic-ray showers, the longitudinal position of the reconstructed vertex was required to be in the range $|Z_{\text{vertex}}| < 40$ cm;

- to remove background due to charged current DIS events and cosmic-ray showers, a cut on the relative transverse momentum of $p_T/\sqrt{E_T} < 1.5\sqrt{\text{GeV}}$ was made, where p_T and E_T are, respectively, the measured transverse momentum and transverse energy of the event;
- NC DIS events with a scattered positron candidate in the CAL were removed by cutting [7] on the inelasticity, y , which is estimated from $y_e = 1 - \frac{E'_e}{2E_e}(1 - \cos\theta'_e)$, where E'_e and θ'_e are the energy and polar angle, respectively, of the scattered positron candidate. Events were rejected if $y_e < 0.85$;
- the requirement $0.2 < y_{\text{JB}} < 0.85$ was imposed, where y_{JB} is the estimator of y measured from the CAL energy deposits according to the Jacquet-Blondel method [54]. The upper cut removed NC DIS events where the lepton was not identified and which therefore have a value of y_{JB} close to 1. The lower cut removed proton beam-gas events which have a low value of y_{JB} . These requirements on y_{JB} restrict the photon-proton centre-of-mass energy to be in the range 134 to 277 GeV.

The cuts on y_e and y_{JB} reduced the background from DIS events to less than 0.5% and restricted the range of the virtuality of the exchanged photon to $Q^2 < 1 \text{ GeV}^2$, with a median value of about 10^{-3} GeV^2 . After these requirements, 62573 events with two or more jets remained in the sample; 2919 of these events had a third jet of transverse energy greater than 11 GeV in the range $-1 < \eta^{\text{jet3}} < 2.4$. For the measurements of the cross section as a function of $\cos\theta^*$, the following additional requirements were imposed:

- the dijet scattering angle was restricted to be in the range $|\cos\theta^*| < 0.8$;
- the invariant mass of the two jets of highest transverse energy was required to satisfy $M^{\text{jj}} > 42 \text{ GeV}$;
- the boost of the dijet system was required to be in the range $0.1 < \bar{\eta} < 1.3$.

These cuts reduced the sample to 10811 events.

9 Event characteristics

For the high transverse energies studied here, it has been shown previously [2,4] that the transverse energy flow around jets is generally well described by the simulation. This agreement is maintained in the more-forward region studied here, with PYTHIA giving a description similar to that of HERWIG.

Kinematic distributions in the data are compared to the two simulation programs in Fig. 2. The simulated distributions were fit to the data distribution in x_γ^{obs} , shown in Fig. 2(a), by varying the fractions of direct and resolved processes and minimising the

χ^2 . The simulations generally describe the data well for all variables, although some discrepancies are seen. The shape of the distribution in y_{JB} is better described by the HERWIG prediction, although the description by the PYTHIA simulation is adequate. Both simulations have similar distributions for the transverse energies of the jets and describe the data well. However, neither gives a good description of the pseudorapidity of the jet of highest transverse energy, whereas the pseudorapidity distribution of the second jet is well described by HERWIG. Figure 2 also shows that according to the HERWIG simulation, the proportion of resolved photon events decreases with increasing x_γ^{obs} and E_T^{jet} and increases with increasing y_{JB} and η^{jet} .

Since HERWIG gives a better overall description of the data than PYTHIA, it was chosen as the primary MC generator to correct the data. The correction was performed using the bin-by-bin method, in which the correction factor, as a function of an observable \mathcal{O} in a given bin i , is $C_i(\mathcal{O}) = N_i^{\text{had}}(\mathcal{O})/N_i^{\text{det}}(\mathcal{O})$. The variable $N_i^{\text{had}}(\mathcal{O})$ is the number of events passing the kinematic requirements on the hadronic final state described in Section 4 and $N_i^{\text{det}}(\mathcal{O})$ is the number of reconstructed events passing the selection requirements as detailed in Section 8. Both numbers were computed using the MC generators described in Section 5. For distributions as a function of x_γ^{obs} , the correction factors lie in the range 0.85–1.25.

10 Experimental and theoretical uncertainties

10.1 Experimental uncertainties

The results of a detailed analysis of the possible sources of systematic uncertainty are listed below. Typical values for the systematic uncertainty are quoted for the cross sections as a function of x_γ^{obs} :

- varying the measured jet energies by $\pm 1\%$ in only the simulated sample, in accordance with the uncertainty in the jet energy scale, gave an uncertainty of $\mp 5\%$, increasing with E_T^{jet1} ;
- correcting the data with PYTHIA instead of the HERWIG generator gave an uncertainty within $\pm 9\%$ and typically $\pm 4\%$;
- changing the cuts on E_T^{jet1} and E_T^{jet2} in both the data and simulated samples by the value of the average resolution ($\sim 9\%$) gave an uncertainty of $\pm 5\%$;
- changing the cuts on y_{JB} in both the data and simulated samples by the value of the resolution (~ 0.03 at low y_{JB} and ~ 0.05 at high y_{JB}) gave an uncertainty of less than $\pm 2\%$;

- changing the cuts on $\eta^{\text{jet}1,2}$ in both the data and simulated samples by the value of the resolution (~ 0.04) gave an uncertainty of $\pm 0.5\%$;
- varying the cuts to remove DIS and beam-gas backgrounds in both data and simulated samples gave a total uncertainty of less than $\pm 1\%$.

In addition to the above, the cuts made to evaluate the cross section as a function of $|\cos\theta^*|$ also lead to sources of systematic uncertainty. The following were evaluated, with typical uncertainties quoted:

- changing the cuts on M^{jj} in both the data and simulated samples by the value of the average resolution ($\sim 8\%$) gave an uncertainty of $\pm 5\%$;
- changing the cuts on $\bar{\eta}$ in both the data and simulated samples by the value of the resolution (~ 0.04) gave an uncertainty of $\pm 2\%$;
- changing the cuts on x_γ^{obs} in both the data and simulated samples by the value of the resolution (~ 0.04) gave an uncertainty of $\pm 4\%$. This systematic uncertainty also contributes to the measurements of the cross-sections $d\sigma/dE_T^{\text{jet}1}$ and $d\sigma/d\eta^{\text{jet}2}$.

The uncertainty in the cross sections due to the jet energy scale uncertainty is correlated between bins and is therefore displayed separately as a shaded band in the figures. All other systematic uncertainties were added in quadrature. In addition, an overall normalisation uncertainty of 1.6% from the luminosity determination is not included in either the figures or tables.

As a cross check, cross sections were obtained with an iterative matrix-unfolding technique [55], using Bayes' theorem. The resultant cross sections were found to be consistent with those using the standard bin-by-bin procedure [27].

10.2 Theoretical uncertainties

The NLO QCD predictions for the dijet cross section are affected by the systematic uncertainties listed below. Typical values for the systematic uncertainty are quoted for the cross sections as a function of x_γ^{obs} :

- the uncertainty due to terms beyond NLO, estimated by varying μ between E_T and $E_T/4$, is $\pm(10 - 20)\%$, increasing with decreasing x_γ^{obs} ;
- the uncertainty due to the hadronisation correction, estimated as half the spread between the δ_{had} values obtained using the HERWIG and PYTHIA models, is $\pm(2 - 3)\%$;
- the uncertainty due to the value of $\alpha_s(M_Z)$, estimated by repeating the calculations using the CTEQ4 series of PDFs determined using values of $\alpha_s(M_Z) = 0.113, 0.116$ and 0.119 , is $\pm(5 - 8)\%$.

The above systematic uncertainties are largely independent of the choice of photon PDF and were added in quadrature to give the total uncertainty on the predictions in each case. Differences between parameterisations of the photon and proton parton densities are discussed in the comparison to the measured data in Section 11.

11 Results

11.1 Probing the matrix elements

The dijet cross section as a function of $|\cos\theta^*|$, is given in Table 1 and shown in Fig. 3. The data are shown separately for $x_\gamma^{\text{obs}} < 0.75$ (Fig. 3(a)) and $x_\gamma^{\text{obs}} > 0.75$ (Fig. 3(b)) and compared to NLO predictions. For $x_\gamma^{\text{obs}} < 0.75$, the measured cross section lies above the NLO prediction using GRV-HO for the photon PDF by an average of (10 – 15)%. Considering the theoretical and experimental uncertainties, both of (5 – 10)%, the NLO prediction gives a reasonable description of the data. The predictions using the AFG-HO parameterisation for the photon give a lower cross section than that of GRV-HO, and are thus around (20 – 25)% lower than the data. For $x_\gamma^{\text{obs}} > 0.75$, the NLO prediction is in agreement with the measured cross section.

In Fig. 3(c), the shapes of the data and NLO distributions are compared. The predictions give a generally good description of the data; the shapes of the predictions when using the GRV-HO and AFG-HO parameterisations are similar. The data at low x_γ^{obs} rise more rapidly at high $|\cos\theta^*|$ than those at high x_γ^{obs} . This is consistent with a difference in the dominant propagators, as observed in a previous publication [5]; this is seen here at higher energies and masses. The agreement in shape of these distributions, which are sensitive to the matrix elements, demonstrates that also in this high-mass region the dynamics of the short-distance process is understood.

11.2 Cross sections in E_T^{jet1} and η^{jet2}

Measurements of the dijet cross section as a function of E_T^{jet1} are given in Tables 2 and 3 and shown in Figs. 4–7, in different regions of the pseudorapidities of the two jets for $x_\gamma^{\text{obs}} > 0.75$ and $x_\gamma^{\text{obs}} < 0.75$. The ratios of the cross sections to theory are shown in Figs. 5 and 7. In Fig. 4, the measurement for $x_\gamma^{\text{obs}} > 0.75$ extends to transverse energies of ~ 70 GeV, extending the region measured previously [2]. In general, the overall description of the data by the predictions is reasonable. In particular, when the jets are produced in the region $1 < \eta^{\text{jet1}} < 2.4$ and $0 < \eta^{\text{jet2}} < 1$, the cross section in Fig. 4 falls three orders of magnitude and is well described by the NLO calculation. When both jets are produced

in the region $1 < \eta^{\text{jet}1,2} < 2.4$, the NLO prediction lies below the data at low transverse energy, although both the experimental and theoretical uncertainties are sizeable. In this region, the hadronisation corrections are significant but do not account for all the differences. This region is near the edge of phase space due to the cuts applied.

At low x_γ^{obs} (Figs. 6 and 7), the data are also generally well described by the NLO predictions, although a difference in shape is seen, with the predictions lying above the data at low transverse energy and below for $E_T^{\text{jet}1} > 20$ GeV. The predictions using AFG-HO are uniformly about 15% below those of GRV-HO for the entire range of transverse energies.

The pseudorapidities of the two jets are sensitive to the momentum distributions of the incoming partons. The cross section is measured as a function of the pseudorapidity of one of the jets, in different regions of pseudorapidity of the other, and is shown at high x_γ^{obs} (Fig. 8) and low x_γ^{obs} (Fig. 9). The NLO predictions give a good description of the data except for $-1 < \eta^{\text{jet}1} < 0$ for low x_γ^{obs} , where the data are at or below the lower edge of the scale-uncertainty band. The predictions using AFG-HO lie about (10 – 15)% below those of GRV-HO.

11.3 Testing the current parameterisations of the photon PDF

The cross sections and ratios of data and theory as a function of x_γ^{obs} in regions of increasing transverse energy are shown in Figs. 10–12. The predictions lie significantly above the data using the GRV-HO parameterisation at the lowest values ($14 < E_T^{\text{jet}1} < 17$ GeV) of transverse energy for $x_\gamma^{\text{obs}} > 0.5$, but are increasingly below the data for values larger than 17 GeV. This trend with transverse energy is stronger for $x_\gamma^{\text{obs}} < 0.8$, as can be seen in Fig. 11. Given the uncertainties, the data and predictions are consistent except in the region of lowest transverse energy for $x_\gamma^{\text{obs}} > 0.5$. The dominant theoretical uncertainty, estimated from the variation of the renormalisation and factorisation scales, arises from the higher-order contributions not present in an NLO calculation. The inclusion of higher-order contributions would have to result in a significant change of shape of the distribution as a function of both the transverse energy and x_γ^{obs} if it were to describe the data. The data in Fig. 10 are also compared to the NLO prediction using the AFG-HO photon parameterisation; the ratio of data to the theory is shown in Fig. 12. The prediction agrees with the data in the region of lowest transverse energy, but is below the data for the higher $E_T^{\text{jet}1}$ bins. The predictions using AFG-HO are similar in shape to those using GRV-HO but are (10 – 15)% lower. Figures 11 and 12 also show the predictions using the MRST99 PDFs in the proton. The differences between the predictions with CTEQ5M1 and MRST99 are everywhere less than 5%.

11.4 Discussion

To improve the understanding of the features of the cross section in different regions of transverse energy, the sensitivity of the above comparisons to the value of the cut on the second jet has been studied. Starting at a minimum of 11 GeV, the cut on the second jet was raised in both data and theory for the region $25 < E_T^{\text{jet1}} < 35$ GeV; the results are shown in Fig. 13. With increasing $E_T^{\text{jet2,cut}}$, the data fall, as expected; the trend is well reproduced by the HERWIG simulation, which includes leading-logarithmic parton showers. The prediction from HERWIG is normalised to the data in the first bin in Fig. 13(a). The LO prediction (not shown) for this cross section is flat, since only two partons are emitted, which must have equal transverse energies by conservation of energy. The predictions of the shape of this distribution from $\mathcal{O}(\alpha\alpha_s^2)$ QCD are therefore the lowest non-trivial order predictions. The predictions from NLO QCD are shown; they fall less rapidly at low $E_T^{\text{jet2,cut}}$ and more rapidly at high $E_T^{\text{jet2,cut}}$ than the data. Frixione and Ridolfi [41] have shown that, when the requirements on the minimum transverse energy of the two jets are similar, the NLO calculation is infrared sensitive. This has been investigated further by considering the cross section for regions of high and low x_γ^{obs} . For $x_\gamma^{\text{obs}} > 0.8$, shown in Fig. 13(b), the data and NLO QCD converge for low $E_T^{\text{jet2,cut}}$, both being reasonably insensitive to the cut and similar in shape. From Fig. 13, it can be seen that for a cut on the first jet of $25 < E_T^{\text{jet1}} < 35$ GeV, the cut on the jet of lower transverse energy has to be below 21 GeV for the NLO predictions to agree with the data. Figure 13(c) shows the region $x_\gamma^{\text{obs}} < 0.8$; the predictions lie below the data at low $E_T^{\text{jet2,cut}}$, but within the theoretical uncertainties. The prediction using AFG-HO is about (10 – 15)% below that of GRV-HO, but is similar in shape and is therefore just compatible with the data.

The difference in the behaviour of the data and the calculations in Fig. 13 implies that there is a significant dependence on $E_T^{\text{jet2,cut}}$ in the comparisons between the measurements in the previous section and NLO QCD. By adjusting $E_T^{\text{jet2,cut}}$ separately in each E_T^{jet1} range, it would be possible to achieve agreement between the NLO prediction and the data. However, this seems to be a somewhat arbitrary procedure.

The agreement with theory at high x_γ^{obs} and high transverse energy, where the dependence on the photon structure is small, demonstrates a consistency between these data and the gluon distribution in the proton extracted from DIS data. Further discrimination between the current PDFs is currently not possible given the large uncertainties in the theory at low transverse energies and both the experimental and theoretical uncertainties at higher transverse energies. However, the data shown here significantly constrain the parton densities in the photon. These constraints would be made more stringent with improved higher-order, or resummed, calculations.

12 Conclusions

The dijet cross section in photoproduction has been measured in the kinematic region $Q^2 < 1 \text{ GeV}^2$, $0.2 < y < 0.85$, $E_T^{\text{jet}1} > 14 \text{ GeV}$, $E_T^{\text{jet}2} > 11 \text{ GeV}$ and $-1 < \eta^{\text{jet}1,2} < 2.4$. In the high-mass region defined by $M^{\text{jj}} > 42 \text{ GeV}$ and $0.1 < \bar{\eta} < 1.3$, the dijet angular distribution of the data is well reproduced by the NLO predictions, indicating that the dynamics of the short-distance process is understood. Over the wider region, the measurements are compared with NLO predictions using different parameterisations for the parton densities of the photon. The data fall less steeply with increasing transverse energy than do the NLO QCD predictions, and show sensitivity to the parton densities of the photon. Neither the AFG-HO nor the GRV-HO parameterisation, convoluted with the NLO matrix elements, fully describes all features of the data. There is agreement with theory at high x_γ^{obs} and high transverse energy, where the dependence on the photon structure is small, which represents a consistency check of the gluon distribution in the proton extracted from deep inelastic scattering. The data at low x_γ^{obs} significantly constrain the parton densities in the photon; future parameterisations of the photon PDFs should take them into account. These constraints would be made more stringent were improved higher-order or resummed calculations available.

Acknowledgements

The design, construction and installation of the ZEUS detector have been made possible by the ingenuity and dedicated efforts of many people from inside DESY and from the home institutes who are not listed as authors. Their contributions are acknowledged with great appreciation. The experiment was made possible by the inventiveness and the diligent efforts of the HERA machine group. The strong support and encouragement of the DESY directorate have been invaluable. We thank S. Frixione and G. Ridolfi for making their NLO code freely available and S. Frixione, in particular, for answering many questions on how to use the code and on jet photoproduction in general. We also thank M. H. Seymour and M. Klasen for useful discussions.

References

- [1] H1 Collab., C. Adloff et al., Phys. Lett. **B 483**, 36 (2000);
H1 Collab., C. Adloff et al., Eur. Phys. J. **C 1**, 97 (1998);
H1 Collab., S. Aid et al., Z. Phys. **C 70**, 17 (1996);
H1 Collab., I. Abt et al., Phys. Lett. **B 314**, 436 (1993).
- [2] ZEUS Collab., J. Breitweg et al., Eur. Phys. J. **C 11**, 35 (1999).
- [3] ZEUS Collab., J. Breitweg et al., Phys. Lett. **B 443**, 394 (1998).
- [4] ZEUS Collab., J. Breitweg et al., Eur. Phys. J. **C 1**, 109 (1998).
- [5] ZEUS Collab., M. Derrick et al., Phys. Lett. **B 384**, 401 (1996).
- [6] ZEUS Collab., M. Derrick et al., Phys. Lett. **B 348**, 665 (1995).
- [7] ZEUS Collab., M. Derrick et al., Phys. Lett. **B 322**, 287 (1994).
- [8] ZEUS Collab., J. Breitweg et al., Eur. Phys. J. **C 18** (2001);
ZEUS Collab., J. Breitweg et al., Eur. Phys. J. **C 6**, 67 (1999);
ZEUS Collab., J. Breitweg et al., Eur. Phys. J. **C 4**, 591 (1998);
ZEUS Collab., M. Derrick et al., Phys. Lett. **B 342**, 417 (1995).
- [9] BCDMS Collab., A.C. Benvenuti et al., Phys. Lett. **B 223**, 485 (1989);
NMC Collab., M. Arneodo et al., Nucl. Phys. **B 483**, 3 (1997);
H1 Collab., C. Adloff et al., Eur. Phys. J. **C 21**, 33 (2001);
ZEUS Collab., S. Chekanov et al., Eur. Phys. J. **C 21**, 443 (2001).
- [10] JADE Collab., W. Bartel et al., Z. Phys. **C 24**, 231 (1984).
- [11] TASSO Collab., M. Althoff et al., Z. Phys. **C 31**, 527 (1986).
- [12] PLUTO Collab., C. Berger et al., Nucl. Phys. **B 281**, 365 (1987).
- [13] TPC/Two-Gamma Collab., H. Aihara et al., Z. Phys. **C 34**, 1 (1987).
- [14] OPAL Collab., G. Abbiendi et al., Eur. Phys. J. **C 18**, 15 (2000);
OPAL Collab., K. Ackerstaff et al., Phys. Lett. **B 411**, 387 (1997);
OPAL Collab., R. Akers et al., Z. Phys. **C 61**, 199 (1994);
OPAL Collab., K. Ackerstaff et al., Z. Phys. **C 74**, 33 (1997);
OPAL Collab., K. Ackerstaff et al., Phys. Lett. **B 412**, 225 (1997).
- [15] DELPHI Collab., P. Abreu et al., Z. Phys. **C 69**, 223 (1996).
- [16] L3 Collab., M. Acciarri et al., Phys. Lett. **B 436**, 403 (1998);
L3 Collab., M. Acciarri et al., Phys. Lett. **B 447**, 147 (1999).
- [17] H1 Collab., C. Adloff et al., Report DESY-01-225, DESY (2001).
- [18] H. Baer, J. Ohnemus and J. F. Owens, Phys. Rev. **D 40**, 2844 (1989).

- [19] ZEUS Collab., M. Derrick et al., Phys. Lett. **B 297**, 404 (1992).
- [20] ZEUS Collab., U. Holm (ed.), *The ZEUS Detector*. Status Report (unpublished), DESY (1993), available on <http://www-zeus.desy.de/bluebook/bluebook.html>.
- [21] M. Derrick et al., Nucl. Instr. and Meth. **A 309**, 77 (1991);
A. Andresen et al., Nucl. Instr. and Meth. **A 309**, 101 (1991);
A. Bernstein et al., Nucl. Instr. and Meth. **A 336**, 23 (1993);
A. Caldwell et al., Nucl. Instr. and Meth. **A 321**, 356 (1992).
- [22] N. Harnew et al., Nucl. Instr. and Meth. **A 279**, 290 (1989);
B. Foster et al., Nucl. Phys. Proc. Suppl. **B 32**, 181 (1993);
B. Foster et al., Nucl. Instr. and Meth. **A 338**, 254 (1994).
- [23] J. Andruszków et al., Report DESY-92-066, DESY (1992);
ZEUS Collab., M. Derrick et al., Z. Phys. **C 63**, 391 (1994);
J. Andruszków et al., Preprint DESY-01-141, DESY (2001).
- [24] S. Catani, Yu. L. Dokshitzer and B. Webber, Nucl. Phys. **B 406**, 187 (1993).
- [25] S.D. Ellis and D.E. Soper, Phys. Rev. **D 48**, 3160 (1993).
- [26] W. T. Giele, E. W. N. Glover and D. A. Kosower, Phys. Rev. Lett. **73**, 2019 (1994).
- [27] E. A. Heaphy, *Jet photoproduction and photon structure*. Ph.D. Thesis, University College London (2001), (unpublished), available on <http://www.hep.ucl.ac.uk/theses/>.
- [28] G. Marchesini et al., Comp. Phys. Comm. **67**, 465 (1992).
- [29] T. Sjöstrand, Comp. Phys. Comm. **82**, 74 (1994).
- [30] B. R. Webber, Nucl. Phys. **B 238**, 492 (1984).
- [31] B. Andersson et al., Phys. Rep. **97**, 31 (1983).
- [32] R. Brun et al., GEANT3, Technical Report CERN-DD/EE/84-1, CERN, 1987.
- [33] N. H. Brook et al., *Proc. the Workshop on Future Physics at HERA*, G. Ingleman, A. De Roeck and R. Klanner (eds.), Vol. 1, p. 613. DESY (1996).
- [34] M. Glück, E. Reya and A. Vogt, Phys. Rev. **D 45**, 3986 (1992);
M. Glück, E. Reya and A. Vogt, Phys. Rev. **D 46**, 1973 (1992).
- [35] H.L. Lai et al., Phys. Rev. **D 55**, 1280 (1997).
- [36] J. M. Butterworth and R. J. Taylor, *International Conference on the Structure and Interactions of the Photon (Photon 99)*, Freiburg, Germany, 23-27 May 1999, Vol. 82, p. 112. Nucl. Phys. Proc. Suppl. (2000). Also in preprint hep-ph/9907394.
- [37] G. A. Schuler and T. Sjöstrand, Phys. Lett. **B 376**, 193 (1996).

- [38] M. Glück, E. Reya and A. Vogt, *Z. Phys.* **C 67**, 433 (1995).
- [39] T. Sjöstrand and M. van Zijl, *Phys. Rev.* **D 36**, 2019 (1987).
- [40] S. Frixione, Z. Kunszt and A. Signer, *Nucl. Phys.* **B 467**, 399 (1996);
S. Frixione, *Nucl. Phys.* **B 507**, 295 (1997).
- [41] S. Frixione and G. Ridolfi, *Nucl. Phys.* **B 507**, 315 (1997).
- [42] B. W. Harris and J. F. Owens, *Phys. Rev.* **D 56**, 4007 (1997).
- [43] B. W. Harris and J. F. Owens, *Phys. Rev.* **D 57**, 5555 (1998).
- [44] M. Klasen and G. Kramer, *Z. Phys.* **C 76**, 67 (1997).
- [45] M. Klasen, T. Kleinwort and G. Kramer, *Eur. Phys. J.* **direct C 1**, 1 (1998).
- [46] P. Aurenche et al., *Eur. Phys. J.* **C 17**, 413 (2000).
- [47] B. W. Harris, M. Klasen and J. Vossebeld, *Proc. Workshop on Monte Carlo Generators for HERA Physics*, T.A. Doyle et al. (ed.), p. 171. DESY, Hamburg, Germany (1999). Also in preprint DESY-PROC-1999-02, available on <http://www.desy.de/~heramc/>.
- [48] R. K. Ellis, D. A. Ross and A. E. Terrano, *Nucl. Phys.* **B 178**, 421 (1981).
- [49] L. E. Gordon and J. K. Storrow, *Nucl. Phys.* **B 489**, 405 (1997).
- [50] A. Vogt, *International Conference on the Structure and Interactions of the Photon (Photon 97), Egmond aan Zee, The Netherlands, May 1997*, p. 3. World Sci. (1998). Also in preprint hep-ph/9709345.
- [51] P. Aurenche, J. Guillet and M. Fontannaz, *Z. Phys.* **C 64**, 621 (1994).
- [52] G. M. Briskin, *Diffraction dissociation in ep deep inelastic scattering*. Ph.D. Thesis, Tel Aviv University (1998), Report DESY-THESIS-1999-036.
- [53] A. H. Ochs, *Dijet photoproduction at high transverse energies with ZEUS at HERA*. Ph.D. Thesis, McGill University, Montreal (2001). In preparation.
- [54] F. Jacquet and A. Blondel, *Proceedings of the Study for an ep Facility for Europe*, U. Amaldi (ed.), p. 391. Hamburg, Germany (1979). Also in preprint DESY 79/48.
- [55] G. D'Agostini, *Nucl. Instr. and Meth.* **A 362**, 487 (1995).

$ \cos\theta^* $ bin	$d\sigma/d \cos\theta^* $	Δ_{stat}	Δ_{syst}	Δ_{ES}	(pb)	C_{had}
$x_{\gamma}^{\text{obs}} < 0.75$						
0.0, 0.1	44.5	± 3.5	$+1.6$ -3.8	$+2.7$ -2.0		0.994 ± 0.010
0.1, 0.2	40.1	± 3.3	$+3.2$ -2.4	$+2.3$ -1.3		1.027 ± 0.021
0.2, 0.3	48.1	± 3.6	$+2.5$ -3.3	$+2.4$ -2.1		1.006 ± 0.001
0.3, 0.4	54.5	± 3.7	$+4.4$ -0.9	$+2.0$ -2.5		1.022 ± 0.017
0.4, 0.5	83.9	± 4.7	$+2.7$ -5.4	$+4.5$ -3.6		1.008 ± 0.014
0.5, 0.6	115.7	± 5.5	$+1.4$ -4.1	$+4.8$ -4.5		1.028 ± 0.020
0.6, 0.7	205.5	± 7.6	$+14.7$ -4.7	$+8.1$ -10.7		1.024 ± 0.010
0.7, 0.8	406.9	± 11.5	$+9.5$ -32.7	$+16.3$ -15.3		1.031 ± 0.001
$x_{\gamma}^{\text{obs}} > 0.75$						
0.0, 0.1	141.8	± 7.1	$+4.0$ -8.1	$+5.5$ -5.2		0.973 ± 0.003
0.1, 0.2	142.1	± 7.1	$+2.7$ -10.0	$+5.7$ -5.6		0.969 ± 0.010
0.2, 0.3	155.3	± 7.3	$+7.9$ -6.8	$+6.5$ -6.4		0.958 ± 0.016
0.3, 0.4	182.7	± 7.9	$+5.2$ -7.7	$+7.3$ -6.5		0.970 ± 0.007
0.4, 0.5	233.8	± 8.8	$+9.6$ -10.7	$+8.8$ -8.9		0.964 ± 0.006
0.5, 0.6	283.9	± 9.7	$+9.1$ -10.8	$+9.4$ -9.9		0.963 ± 0.008
0.6, 0.7	439.7	± 12.2	$+9.2$ -17.2	$+16.3$ -17.8		0.946 ± 0.020
0.7, 0.8	686.6	± 15.9	$+26.0$ -18.3	$+24.8$ -22.6		0.933 ± 0.020

Table 1: Measured cross sections as a function of $|\cos\theta^*|$ for $x_{\gamma}^{\text{obs}} < 0.75$ and $x_{\gamma}^{\text{obs}} > 0.75$. The statistical, systematic and jet energy scale, Δ_{ES} , uncertainties are shown separately. The multiplicative hadronisation correction applied to the NLO prediction is shown in the last column. The uncertainty shown for the hadronisation correction is half the spread between the values obtained using the HERWIG and PYTHIA models.

E_T^{jet1} bin (GeV)	$d\sigma/dE_T^{\text{jet1}}$	Δ_{stat}	Δ_{syst}	Δ_{ES}	(pb/GeV)	C_{had}
$-1 < \eta^{\text{jet1,2}} < 0$						
14, 17	12.2	± 0.6	$+3.6$ -1.1	$+0.6$ -0.5		0.794 ± 0.034
17, 21	3.0	± 0.3	$+0.4$ -0.6	$+0.1$ -0.1		0.757 ± 0.046
$0 < \eta^{\text{jet1}} < 1, -1 < \eta^{\text{jet2}} < 0$						
14, 17	34.3	± 0.7	$+2.2$ -1.6	$+1.3$ -1.0		0.909 ± 0.024
17, 21	16.0	± 0.4	$+0.5$ -2.0	$+0.7$ -0.5		0.907 ± 0.016
21, 25	4.0	± 0.2	$+0.1$ -0.5	$+0.1$ -0.2		0.863 ± 0.007
25, 29	0.74	± 0.08	$+0.08$ -0.17	$+0.02$ -0.03		0.834 ± 0.013
$0 < \eta^{\text{jet1,2}} < 1$						
14, 17	51.4	± 1.1	$+0.4$ -5.7	$+1.6$ -0.9		0.954 ± 0.030
17, 21	26.1	± 0.7	$+0.7$ -2.1	$+0.9$ -1.0		0.974 ± 0.017
21, 25	12.3	± 0.5	$+0.3$ -1.5	$+0.4$ -0.4		0.973 ± 0.015
25, 29	6.3	± 0.3	$+0.1$ -0.8	$+0.3$ -0.2		0.958 ± 0.021
29, 35	1.7	± 0.1	$+0.03$ -0.2	$+0.1$ -0.1		0.953 ± 0.003
35, 41	0.56	± 0.08	$+0.02$ -0.08	$+0.03$ -0.02		0.920 ± 0.006
41, 48	0.122	± 0.037	$+0.031$ -0.014	$+0.003$ -0.010		0.872 ± 0.044
$1 < \eta^{\text{jet1}} < 2.4, -1 < \eta^{\text{jet2}} < 0$						
14, 17	28.1	± 0.6	$+3.4$ -0.7	$+1.0$ -1.1		0.913 ± 0.015
17, 21	15.8	± 0.4	$+0.3$ -1.2	$+0.6$ -0.6		0.922 ± 0.028
21, 25	5.4	± 0.2	$+0.2$ -0.1	$+0.2$ -0.1		0.922 ± 0.012
25, 29	1.6	± 0.1	$+0.2$ -0.1	$+0.1$ -0.1		0.923 ± 0.012
29, 35	0.41	± 0.05	$+0.02$ -0.05	$+0.01$ -0.02		0.862 ± 0.014
35, 41	0.043	± 0.014	$+0.013$ -0.013	$+0.004$ -0.003		0.827 ± 0.004

Table 2: Measured cross section as a function of E_T^{jet1} for events with $x_\gamma^{\text{obs}} > 0.75$. The measurement is divided into six regions of the pseudorapidities of the jets. For further details, see the caption to Table 1.

E_T^{jet1} bin (GeV)	$d\sigma/dE_T^{\text{jet1}}$	Δ_{stat}	Δ_{syst}	Δ_{ES}	(pb/GeV)	C_{had}
$1 < \eta^{\text{jet1}} < 2.4, 0 < \eta^{\text{jet2}} < 1$						
14, 17	38.9	± 0.7	$^{+0.4}_{-2.2}$	$^{+1.1}_{-1.1}$		0.990 ± 0.010
17, 21	23.1	± 0.4	$^{+0.2}_{-1.2}$	$^{+0.8}_{-0.9}$		0.978 ± 0.011
21, 25	11.2	± 0.3	$^{+0.1}_{-0.6}$	$^{+0.4}_{-0.3}$		0.967 ± 0.017
25, 29	5.3	± 0.2	$^{+0.03}_{-0.2}$	$^{+0.2}_{-0.2}$		0.969 ± 0.015
29, 35	2.1	± 0.1	$^{+0.01}_{-0.06}$	$^{+0.1}_{-0.1}$		0.962 ± 0.022
35, 41	0.87	± 0.07	$^{+0.06}_{-0.05}$	$^{+0.06}_{-0.03}$		0.971 ± 0.016
41, 48	0.34	± 0.04	$^{+0.01}_{-0.02}$	$^{+0.02}_{-0.02}$		0.982 ± 0.009
48, 55	0.13	± 0.03	$^{+0.01}_{-0.03}$	$^{+0.01}_{-0.01}$		0.954 ± 0.023
55, 65	0.035	± 0.011	$^{+0.000}_{-0.014}$	$^{+0.002}_{-0.002}$		0.974 ± 0.032
$1 < \eta^{\text{jet1,2}} < 2.4$						
14, 17	1.5	± 0.2	$^{+0.4}_{-0.4}$	$^{+0.0}_{-0.1}$		1.302 ± 0.225
17, 21	4.0	± 0.2	$^{+0.8}_{-0.5}$	$^{+0.2}_{-0.2}$		1.190 ± 0.032
21, 25	5.0	± 0.3	$^{+0.3}_{-0.1}$	$^{+0.2}_{-0.2}$		1.083 ± 0.032
25, 29	3.3	± 0.2	$^{+0.3}_{-0.2}$	$^{+0.1}_{-0.1}$		1.017 ± 0.030
29, 35	1.9	± 0.1	$^{+0.1}_{-0.1}$	$^{+0.0}_{-0.1}$		1.010 ± 0.012
35, 41	0.93	± 0.10	$^{+0.04}_{-0.03}$	$^{+0.08}_{-0.02}$		0.992 ± 0.009
41, 48	0.41	± 0.06	$^{+0.06}_{-0.02}$	$^{+0.02}_{-0.03}$		0.982 ± 0.018
48, 55	0.23	± 0.05	$^{+0.03}_{-0.04}$	$^{+0.01}_{-0.01}$		1.000 ± 0.018
55, 65	0.033	± 0.015	$^{+0.029}_{-0.008}$	$^{+0.002}_{-0.002}$		0.999 ± 0.004
65, 75	0.041	± 0.017	$^{+0.004}_{-0.010}$	$^{+0.002}_{-0.002}$		0.987 ± 0.014

Table 2: (cont.)

E_T^{jet1} bin (GeV)	$d\sigma/dE_T^{\text{jet1}}$	Δ_{stat}	Δ_{syst}	Δ_{ES}	(pb/GeV)	C_{had}
$-1 < \eta^{\text{jet1,2}} < 0$						
14, 17	0.30	± 0.08	$+0.07$ -0.04	$+0.01$ -0.01		1.116 ± 0.130
$0 < \eta^{\text{jet1}} < 1, -1 < \eta^{\text{jet2}} < 0$						
14, 17	6.2	± 0.3	$+0.9$ -0.3	$+0.2$ -0.1		1.006 ± 0.003
17, 21	2.1	± 0.1	$+0.1$ -0.4	$+0.1$ -0.1		1.014 ± 0.012
21, 25	0.23	± 0.04	$+0.05$ -0.06	$+0.01$ -0.01		1.013 ± 0.027
25, 29	0.032	± 0.015	$+0.019$ -0.004	$+0.003$ -0.003		0.888 ± 0.001
$0 < \eta^{\text{jet1,2}} < 1$						
14, 17	29.4	± 0.8	$+0.4$ -1.9	$+1.1$ -1.1		1.006 ± 0.013
17, 21	12.7	± 0.4	$+0.4$ -1.4	$+0.5$ -0.5		1.006 ± 0.005
21, 25	4.6	± 0.3	$+0.2$ -0.5	$+0.3$ -0.2		1.004 ± 0.014
25, 29	1.2	± 0.1	$+0.2$ -0.1	$+0.10$ -0.04		0.972 ± 0.020
29, 35	0.21	± 0.04	$+0.07$ -0.02	$+0.02$ -0.01		1.043 ± 0.038
$1 < \eta^{\text{jet1}} < 2.4, -1 < \eta^{\text{jet2}} < 0$						
14, 17	15.4	± 0.4	$+2.3$ -0.5	$+0.8$ -0.5		1.040 ± 0.019
17, 21	6.0	± 0.2	$+0.5$ -0.1	$+0.3$ -0.3		1.039 ± 0.017
21, 25	1.4	± 0.1	$+0.2$ -0.1	$+0.05$ -0.04		1.007 ± 0.019
25, 29	0.38	± 0.05	$+0.03$ -0.18	$+0.03$ -0.03		1.031 ± 0.017
29, 35	0.057	± 0.015	$+0.013$ -0.022	$+0.001$ -0.001		0.913 ± 0.013
$1 < \eta^{\text{jet1}} < 2.4, 0 < \eta^{\text{jet2}} < 1$						
14, 17	56.7	± 0.8	$+1.6$ -1.0	$+2.1$ -2.1		1.007 ± 0.024
17, 21	26.6	± 0.4	$+0.5$ -0.5	$+1.3$ -1.0		1.021 ± 0.018
21, 25	11.2	± 0.3	$+0.1$ -0.7	$+0.6$ -0.5		1.013 ± 0.014
25, 29	3.7	± 0.2	$+0.1$ -0.2	$+0.1$ -0.2		0.999 ± 0.015
29, 35	1.3	± 0.1	$+0.05$ -0.05	$+0.1$ -0.1		1.003 ± 0.004
35, 41	0.35	± 0.04	$+0.04$ -0.04	$+0.03$ -0.02		1.026 ± 0.009
41, 48	0.064	± 0.016	$+0.007$ -0.009	$+0.003$ -0.005		1.001 ± 0.004
48, 55	0.019	± 0.009	$+0.014$ -0.005	$+0.001$ -0.001		1.000 ± 0.014

Table 3: Measured cross section as a function of E_T^{jet1} for events with $x_\gamma^{\text{obs}} < 0.75$. The measurement is divided into six regions of the pseudorapidities of the jets. For further details, see the caption to Table 1.

E_T^{jet1} bin (GeV)	$d\sigma/dE_T^{\text{jet1}}$	Δ_{stat}	Δ_{syst}	Δ_{ES}	(pb/GeV)	C_{had}
$1 < \eta^{\text{jet1,2}} < 2.4$						
14, 17	78.4	± 1.4	$+6.6$ -5.4	$+2.3$ -2.8		1.000 ± 0.024
17, 21	38.2	± 0.7	$+2.5$ -0.9	$+1.7$ -1.6		1.019 ± 0.025
21, 25	16.9	± 0.5	$+0.9$ -0.3	$+0.8$ -0.7		1.016 ± 0.025
25, 29	6.3	± 0.3	$+0.4$ -0.1	$+0.3$ -0.3		1.012 ± 0.025
29, 35	2.5	± 0.1	$+0.1$ -0.0	$+0.1$ -0.1		1.020 ± 0.032
35, 41	0.92	± 0.08	$+0.05$ -0.01	$+0.09$ -0.06		1.018 ± 0.031
41, 48	0.31	± 0.05	$+0.03$ -0.04	$+0.02$ -0.02		1.000 ± 0.026
48, 55	0.12	± 0.03	$+0.01$ -0.01	$+0.01$ -0.01		0.995 ± 0.019
55, 65	0.045	± 0.016	$+0.014$ -0.016	$+0.004$ -0.003		0.998 ± 0.003

Table 3: (*cont.*)

η^{jet2} bin	$d\sigma/d\eta^{\text{jet2}}$	Δ_{stat}	Δ_{syst}	Δ_{ES}	(pb)	C_{had}
$-1 < \eta^{\text{jet1}} < 0$						
-1.0, -0.5	8.9	± 1.0	$^{+9.5}_{-1.4}$	$^{+0.5}_{-0.8}$		0.538 ± 0.021
-0.5, 0.0	88.2	± 2.8	$^{+15.6}_{-9.2}$	$^{+4.2}_{-3.2}$		0.805 ± 0.031
0.0, 0.5	175.0	± 3.8	$^{+11.1}_{-15.7}$	$^{+5.8}_{-5.7}$		0.881 ± 0.016
0.5, 1.0	195.8	± 4.0	$^{+6.7}_{-12.4}$	$^{+8.5}_{-6.3}$		0.906 ± 0.012
1.0, 1.5	160.3	± 3.4	$^{+9.8}_{-5.0}$	$^{+6.5}_{-5.9}$		0.921 ± 0.012
1.5, 2.0	130.0	± 3.3	$^{+6.9}_{-2.6}$	$^{+4.2}_{-4.7}$		0.913 ± 0.021
2.0, 2.4	89.3	± 3.5	$^{+5.1}_{-5.6}$	$^{+3.6}_{-3.1}$		0.899 ± 0.021
$0 < \eta^{\text{jet1}} < 1$						
-1.0, -0.5	99.3	± 3.1	$^{+11.1}_{-1.9}$	$^{+4.7}_{-2.8}$		0.805 ± 0.012
-0.5, 0.0	272.0	± 4.6	$^{+10.7}_{-26.6}$	$^{+9.8}_{-9.1}$		0.922 ± 0.010
0.0, 0.5	347.0	± 5.1	$^{+3.6}_{-37.8}$	$^{+12.1}_{-10.7}$		0.952 ± 0.015
0.5, 1.0	347.1	± 5.0	$^{+2.2}_{-32.5}$	$^{+11.7}_{-9.2}$		0.960 ± 0.013
1.0, 1.5	287.9	± 4.2	$^{+2.7}_{-19.5}$	$^{+9.3}_{-9.7}$		0.971 ± 0.004
1.5, 2.0	208.1	± 3.7	$^{+1.6}_{-5.4}$	$^{+7.5}_{-7.2}$		0.978 ± 0.012
2.0, 2.4	125.1	± 3.7	$^{+1.9}_{-7.9}$	$^{+3.9}_{-4.3}$		0.967 ± 0.020
$1 < \eta^{\text{jet1}} < 2.4$						
-1.0, -0.5	115.4	± 3.2	$^{+20.5}_{-6.8}$	$^{+5.2}_{-4.8}$		0.866 ± 0.022
-0.5, 0.0	241.7	± 4.2	$^{+6.6}_{-3.5}$	$^{+8.5}_{-8.3}$		0.933 ± 0.011
0.0, 0.5	315.7	± 4.6	$^{+3.8}_{-13.3}$	$^{+11.4}_{-11.2}$		0.953 ± 0.018
0.5, 1.0	277.5	± 4.2	$^{+1.2}_{-18.6}$	$^{+8.5}_{-9.1}$		0.992 ± 0.002
1.0, 1.5	104.0	± 2.4	$^{+4.1}_{-3.5}$	$^{+3.8}_{-4.0}$		1.021 ± 0.007
1.5, 2.0	37.2	± 1.5	$^{+0.8}_{-1.4}$	$^{+1.5}_{-1.3}$		1.018 ± 0.008
2.0, 2.4	13.2	± 1.1	$^{+0.9}_{-2.3}$	$^{+0.5}_{-0.4}$		1.031 ± 0.017

Table 4: Measured cross section as a function of η^{jet2} for events with $x_{\gamma}^{\text{obs}} > 0.75$. The measurement is divided into three regions of the pseudorapidity of the other jet. For further details, see the caption to Table 1.

$\eta^{\text{jet}2}$ bin	$d\sigma/d\eta^{\text{jet}2}$	Δ_{stat}	Δ_{syst}	Δ_{ES}	(pb)	C_{had}
$-1 < \eta^{\text{jet}1} < 0$						
-0.5, 0.0	2.2	± 0.4	$+1.4$ -0.8	$+0.1$ -0.1		1.088 ± 0.113
0.0, 0.5	15.8	± 1.0	$+2.9$ -0.5	$+0.6$ -0.6		1.003 ± 0.019
0.5, 1.0	40.0	± 1.7	$+2.7$ -2.2	$+1.3$ -1.0		1.008 ± 0.008
1.0, 1.5	52.4	± 1.8	$+6.2$ -0.4	$+2.6$ -1.8		1.033 ± 0.027
1.5, 2.0	60.4	± 2.0	$+7.5$ -4.6	$+3.0$ -2.7		1.028 ± 0.002
2.0, 2.4	54.1	± 2.4	$+6.9$ -3.5	$+2.7$ -1.4		1.038 ± 0.024
$0 < \eta^{\text{jet}1} < 1$						
-1.0, -0.5	4.1	± 0.5	$+1.5$ -0.6	$+0.3$ -0.1		1.046 ± 0.020
-0.5, 0.0	51.7	± 1.9	$+4.7$ -2.2	$+1.6$ -1.6		1.004 ± 0.002
0.0, 0.5	131.7	± 3.1	$+3.3$ -11.7	$+6.6$ -5.2		1.002 ± 0.005
0.5, 1.0	195.4	± 3.8	$+4.4$ -14.4	$+7.4$ -7.7		1.002 ± 0.002
1.0, 1.5	230.1	± 3.7	$+4.8$ -11.3	$+9.7$ -9.4		0.998 ± 0.023
1.5, 2.0	262.4	± 4.1	$+5.7$ -4.1	$+11.5$ -10.2		1.012 ± 0.014
2.0, 2.4	243.7	± 5.0	$+6.7$ -7.1	$+10.1$ -9.1		1.020 ± 0.011
$1 < \eta^{\text{jet}1} < 2.4$						
-1.0, -0.5	20.5	± 1.2	$+5.1$ -0.3	$+0.9$ -0.8		1.056 ± 0.020
-0.5, 0.0	135.0	± 3.0	$+13.5$ -5.1	$+6.9$ -5.0		1.028 ± 0.022
0.0, 0.5	288.8	± 4.4	$+5.6$ -6.5	$+12.1$ -11.6		1.016 ± 0.013
0.5, 1.0	403.6	± 5.2	$+9.6$ -9.7	$+17.5$ -15.5		1.006 ± 0.018
1.0, 1.5	403.0	± 4.8	$+24.2$ -15.6	$+16.3$ -16.0		1.008 ± 0.029
1.5, 2.0	355.2	± 4.5	$+27.6$ -20.8	$+13.6$ -14.4		1.013 ± 0.026
2.0, 2.4	305.0	± 5.3	$+27.4$ -11.1	$+11.0$ -10.8		1.015 ± 0.021

Table 5: Measured cross section as a function of $\eta^{\text{jet}2}$ for events with $x_{\gamma}^{\text{obs}} < 0.75$. The measurement is divided into three regions of the pseudorapidity of the other jet. For further details, see the caption to Table 1.

x_γ^{obs} bin	$d\sigma/dx_\gamma^{\text{obs}}$	Δ_{stat}	Δ_{syst}	Δ_{ES} (pb)	C_{had}
$14 < E_T^{\text{jet}1} < 17 \text{ GeV}$					
0.1, 0.2	421.4	± 14.1	$+49.9$ -33.5	$+19.5$ -16.6	0.970 ± 0.002
0.2, 0.3	631.6	± 16.2	$+48.2$ -56.9	$+19.3$ -25.7	0.994 ± 0.027
0.3, 0.4	607.2	± 15.0	$+38.2$ -14.3	$+20.2$ -23.0	0.992 ± 0.022
0.4, 0.5	599.9	± 14.4	$+36.7$ -4.2	$+26.6$ -19.9	1.002 ± 0.023
0.5, 0.6	621.2	± 14.6	$+49.8$ -6.5	$+21.6$ -17.9	1.016 ± 0.026
0.6, 0.7	695.8	± 15.4	$+33.2$ -12.0	$+24.6$ -24.5	1.035 ± 0.014
0.7, 0.8	842.1	± 16.5	$+97.5$ -6.6	$+33.4$ -25.9	1.113 ± 0.002
0.8, 1.0	1784.0	± 18.8	$+128.6$ -78.1	$+57.5$ -52.7	0.906 ± 0.016
$17 < E_T^{\text{jet}1} < 25 \text{ GeV}$					
0.1, 0.2	251.2	± 9.6	$+11.2$ -15.0	$+15.1$ -13.3	1.006 ± 0.019
0.2, 0.3	419.2	± 11.3	$+28.5$ -20.3	$+20.3$ -19.9	1.005 ± 0.013
0.3, 0.4	523.1	± 12.5	$+39.1$ -21.3	$+27.3$ -21.2	1.008 ± 0.019
0.4, 0.5	539.7	± 12.5	$+10.3$ -14.3	$+22.6$ -23.2	1.008 ± 0.012
0.5, 0.6	597.3	± 13.2	$+15.3$ -18.1	$+28.0$ -24.7	1.025 ± 0.018
0.6, 0.7	641.3	± 13.6	$+21.3$ -12.6	$+29.4$ -23.1	1.022 ± 0.019
0.7, 0.8	812.2	± 15.2	$+21.2$ -21.0	$+34.0$ -32.3	1.079 ± 0.002
0.8, 1.0	1791.5	± 17.9	$+30.6$ -154.1	$+65.9$ -62.4	0.933 ± 0.018
$25 < E_T^{\text{jet}1} < 35 \text{ GeV}$					
0.1, 0.4	40.0	± 1.8	$+8.4$ -0.7	$+2.0$ -2.2	1.002 ± 0.025
0.4, 0.6	89.8	± 3.3	$+5.4$ -2.1	$+3.9$ -3.5	1.011 ± 0.011
0.6, 0.8	130.0	± 4.0	$+2.3$ -3.3	$+5.1$ -5.7	1.019 ± 0.021
0.8, 1.0	332.2	± 7.3	$+30.7$ -32.0	$+11.6$ -12.7	0.948 ± 0.016
$35 < E_T^{\text{jet}1} < 90 \text{ GeV}$					
0.1, 0.4	3.9	± 0.6	$+0.4$ -2.0	$+0.3$ -0.2	0.991 ± 0.018
0.4, 0.6	12.7	± 1.2	$+1.1$ -0.3	$+1.1$ -0.8	1.017 ± 0.020
0.6, 0.8	24.5	± 1.7	$+1.3$ -2.5	$+2.2$ -1.3	1.017 ± 0.015
0.8, 1.0	77.6	± 3.6	$+1.6$ -6.1	$+4.5$ -3.3	0.961 ± 0.011

Table 6: Measured cross section as a function of x_γ^{obs} in four regions of $E_T^{\text{jet}1}$. For further details, see the caption to Table 1.

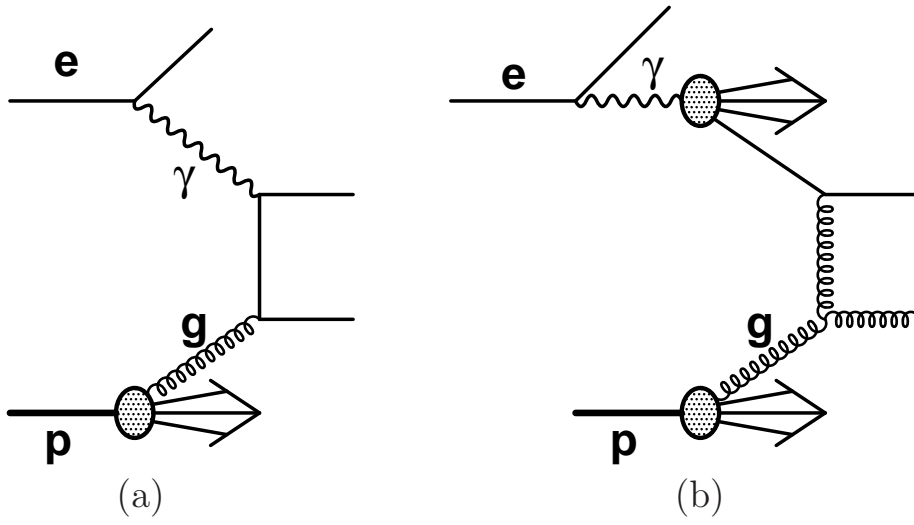


Figure 1: *Examples of (a) direct and (b) resolved dijet photoproduction diagrams in LO QCD.*

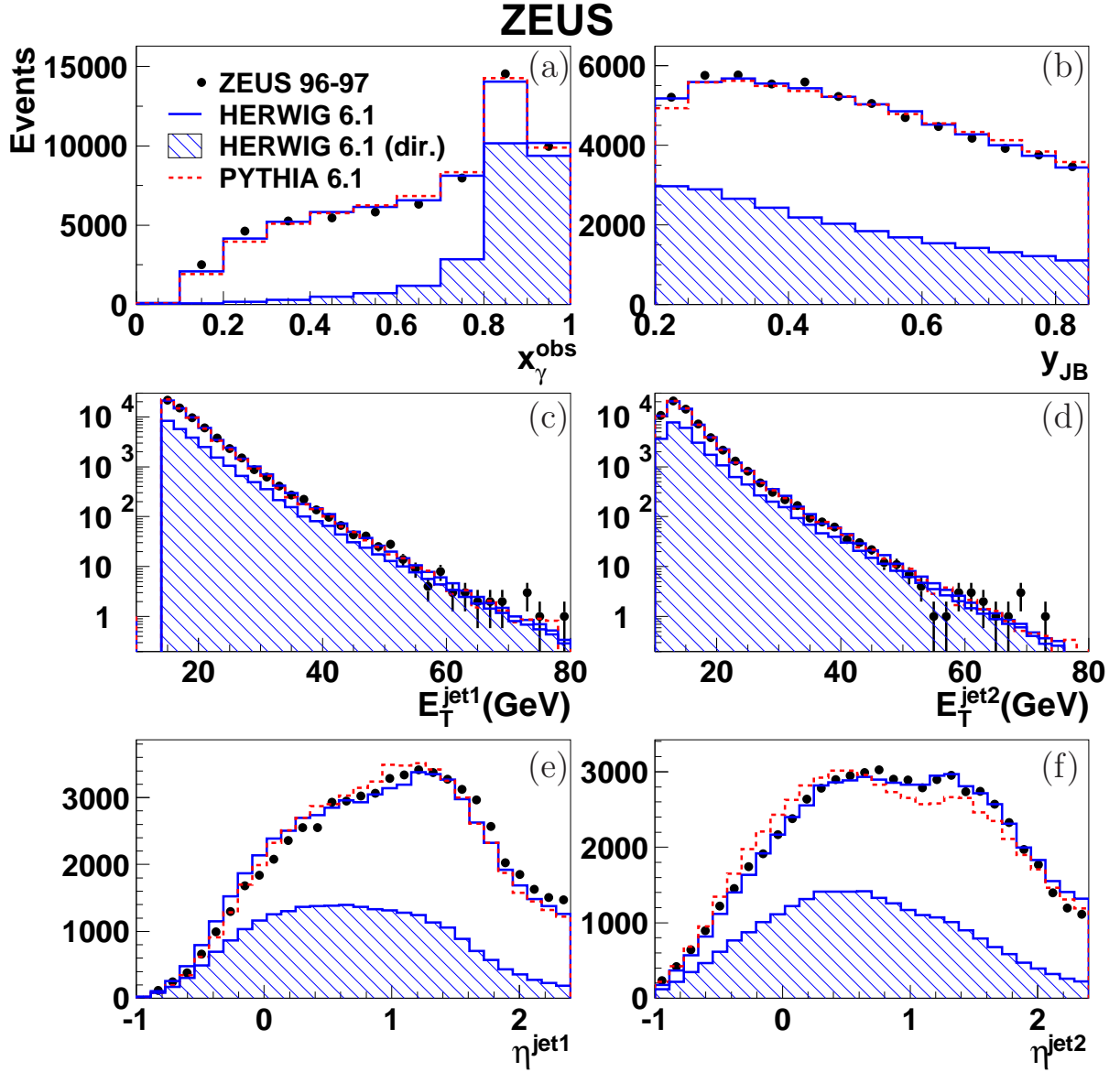


Figure 2: Comparison of data and MC simulation for (a) x_γ^{obs} , (b) y_{JB} , (c) E_T^{jet1} , (d) E_T^{jet2} , (e) η^{jet1} and (f) η^{jet2} . The data are shown as points compared to HERWIG (solid line) and PYTHIA (dashed line). Also shown is the LO component of direct photon processes in HERWIG (hatched area). The simulated sample is normalised to the data and the fraction of direct and resolved photon processes combined according to a χ^2 -fit to the x_γ^{obs} distribution in (a).

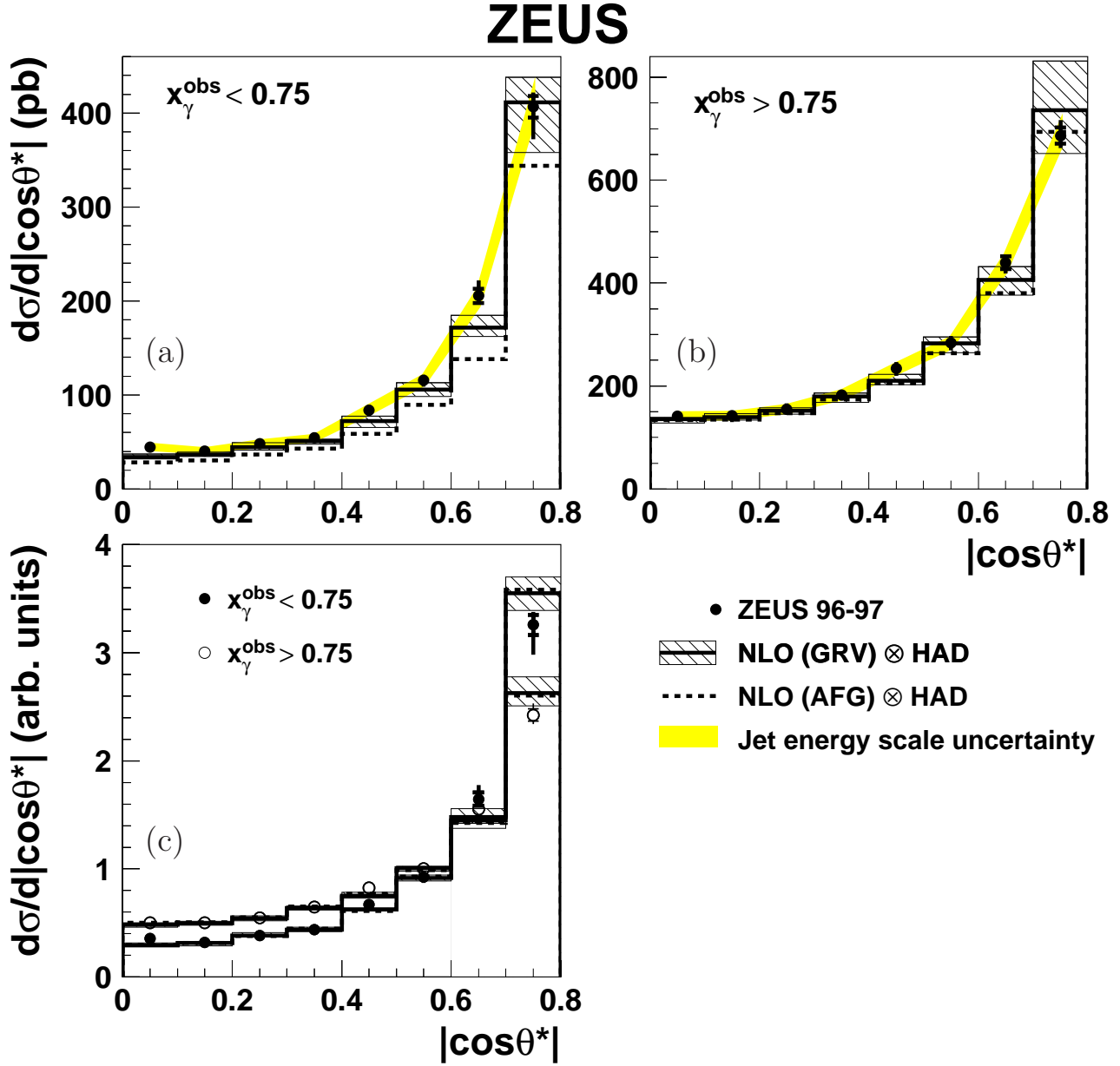


Figure 3: Measured cross sections as a function of $|\cos\theta^*|$ for (a) $x_\gamma^{\text{obs}} < 0.75$ and (b) $x_\gamma^{\text{obs}} > 0.75$, compared to NLO predictions. The data are shown with statistical errors (inner bars) and statistical and systematic uncertainties added in quadrature (outer bars). The uncertainty due to that of the jet energy scale is shown as the shaded band. The NLO prediction corrected for hadronisation effects is shown calculated using the GRV-HO and CTEQ5M1 PDFs for the photon and proton, respectively, and the scale set to $E_T/2$ (solid line). The hatched band represents the quadratic sum of the theoretical uncertainties as discussed in Section 10.2. The prediction using the AFG-HO photon PDF is also shown (dashed line). In (c) the cross sections are area-normalised and the data shown for $x_\gamma^{\text{obs}} < 0.75$ (solid points) and $x_\gamma^{\text{obs}} > 0.75$ (open circles).

ZEUS

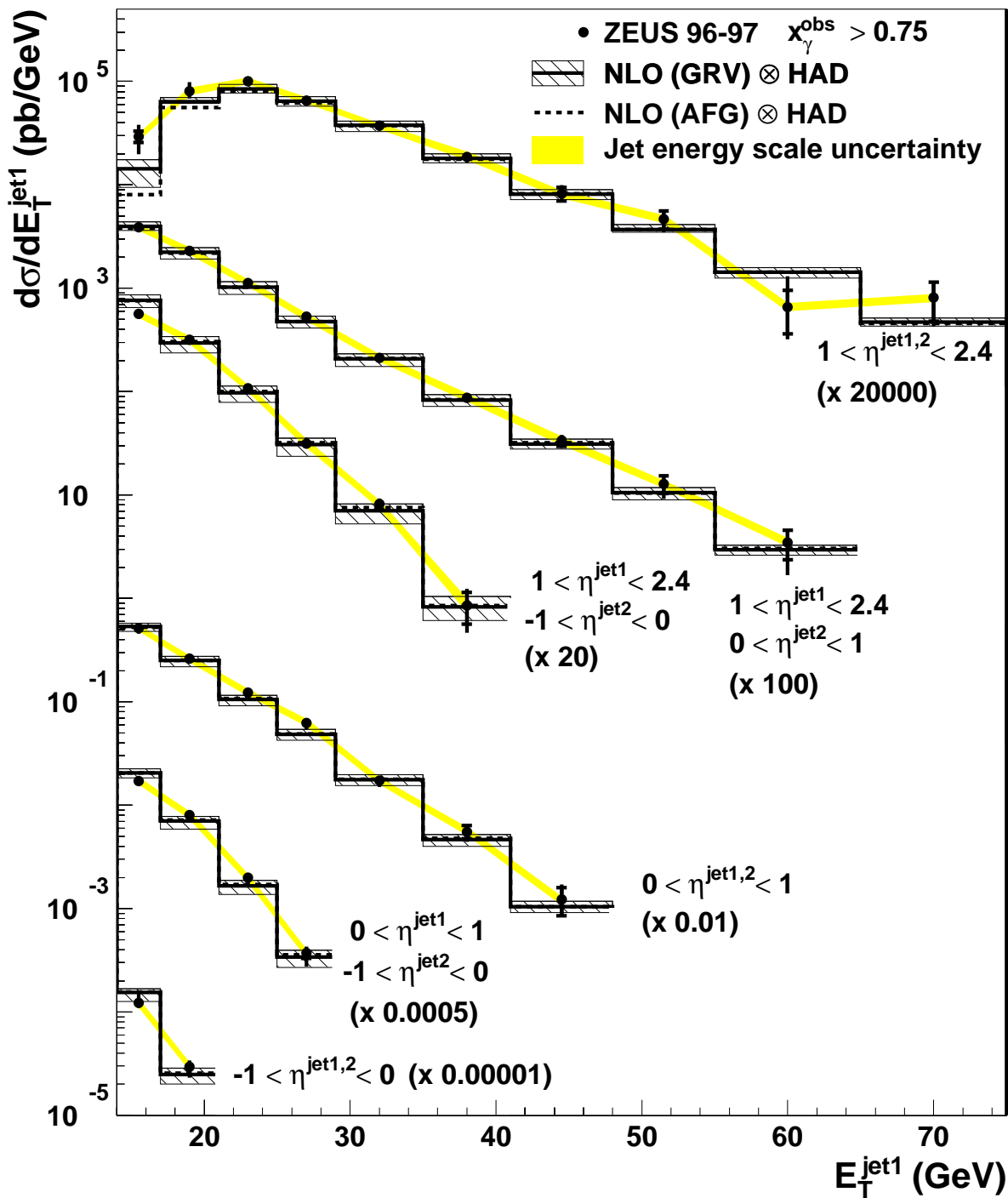


Figure 4: Measured cross section as a function of E_T^{jet1} for events with $x_{\gamma}^{\text{obs}} > 0.75$. The measurement is divided into six regions of the pseudorapidities of the jets. The cross sections are multiplied by the scale factor indicated in brackets so that all regions can be displayed in the same figure. For further details, see the caption to Fig. 3.

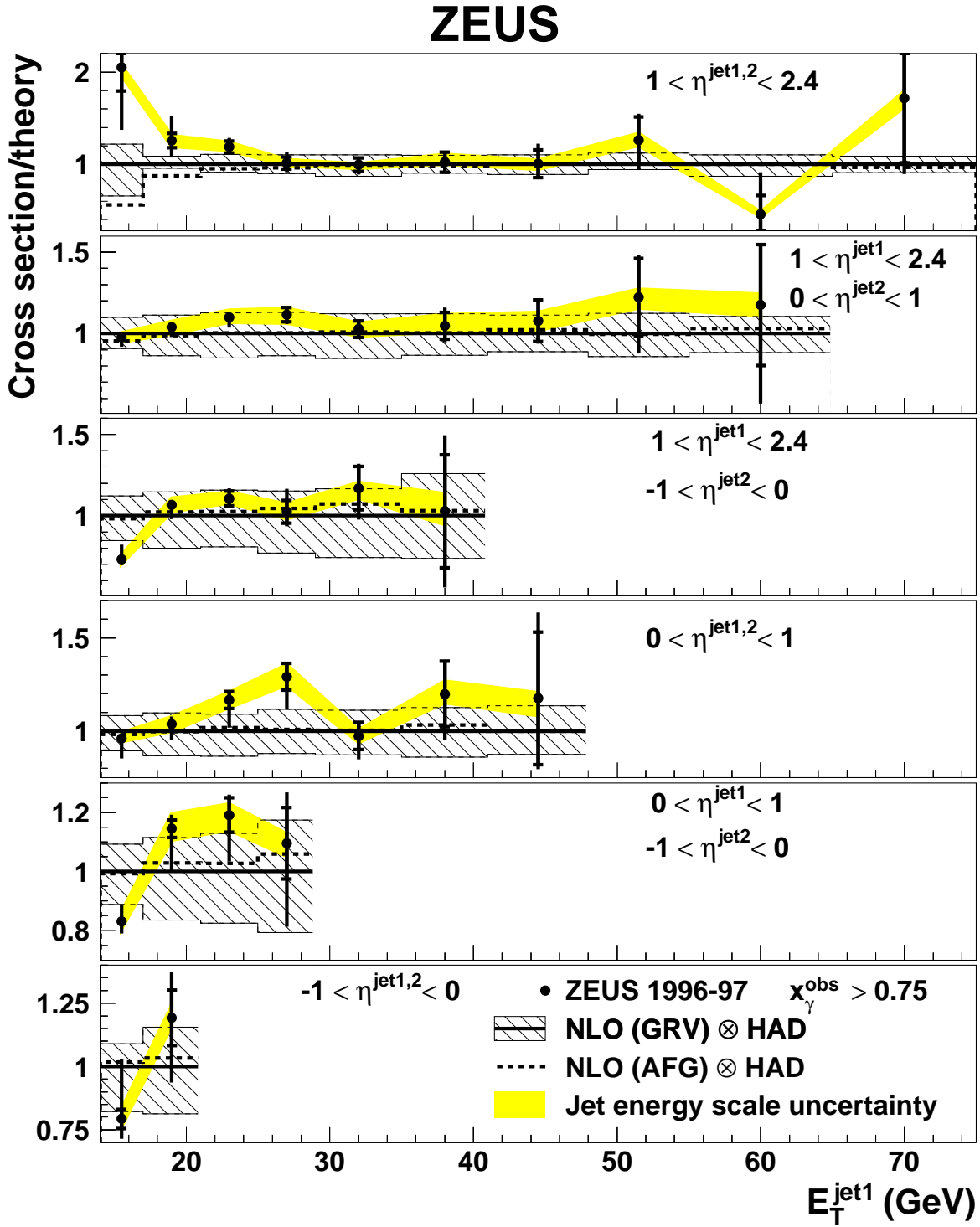


Figure 5: Ratio of cross sections to the central theoretical prediction as a function of $E_T^{\text{jet}1}$ for events with $x_\gamma^{\text{obs}} > 0.75$. The measurement is divided into six regions of the pseudorapidities of the jets. For further details, see the caption to Fig. 3.

ZEUS

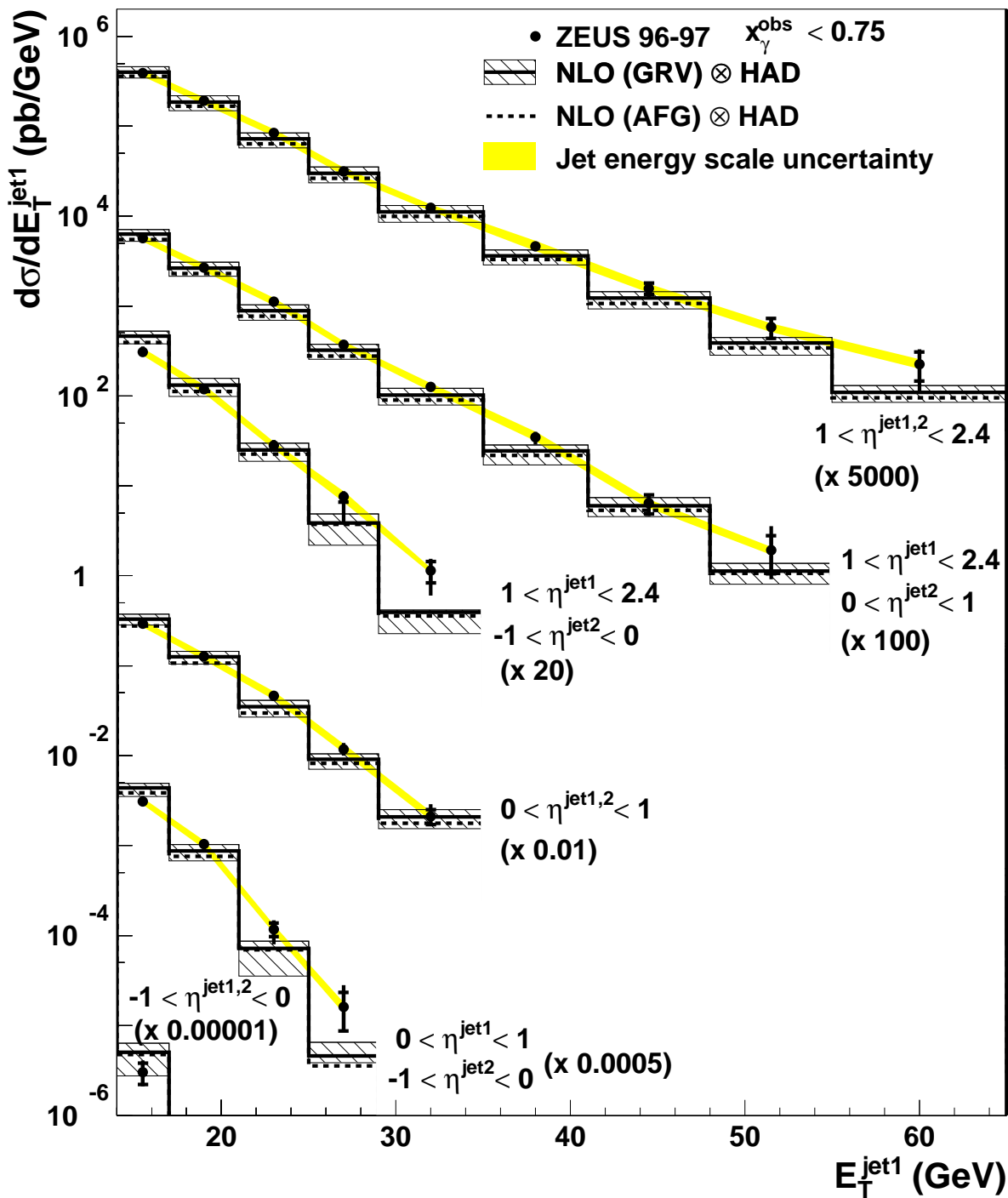


Figure 6: Measured cross section as a function of E_T^{jet1} for events with $x_\gamma^{\text{obs}} < 0.75$. The measurement is divided into six regions of the pseudorapidities of the jets. The cross sections are multiplied by the scale factor indicated in brackets so that all regions can be displayed in the same figures. For further details, see the caption to Fig. 3.

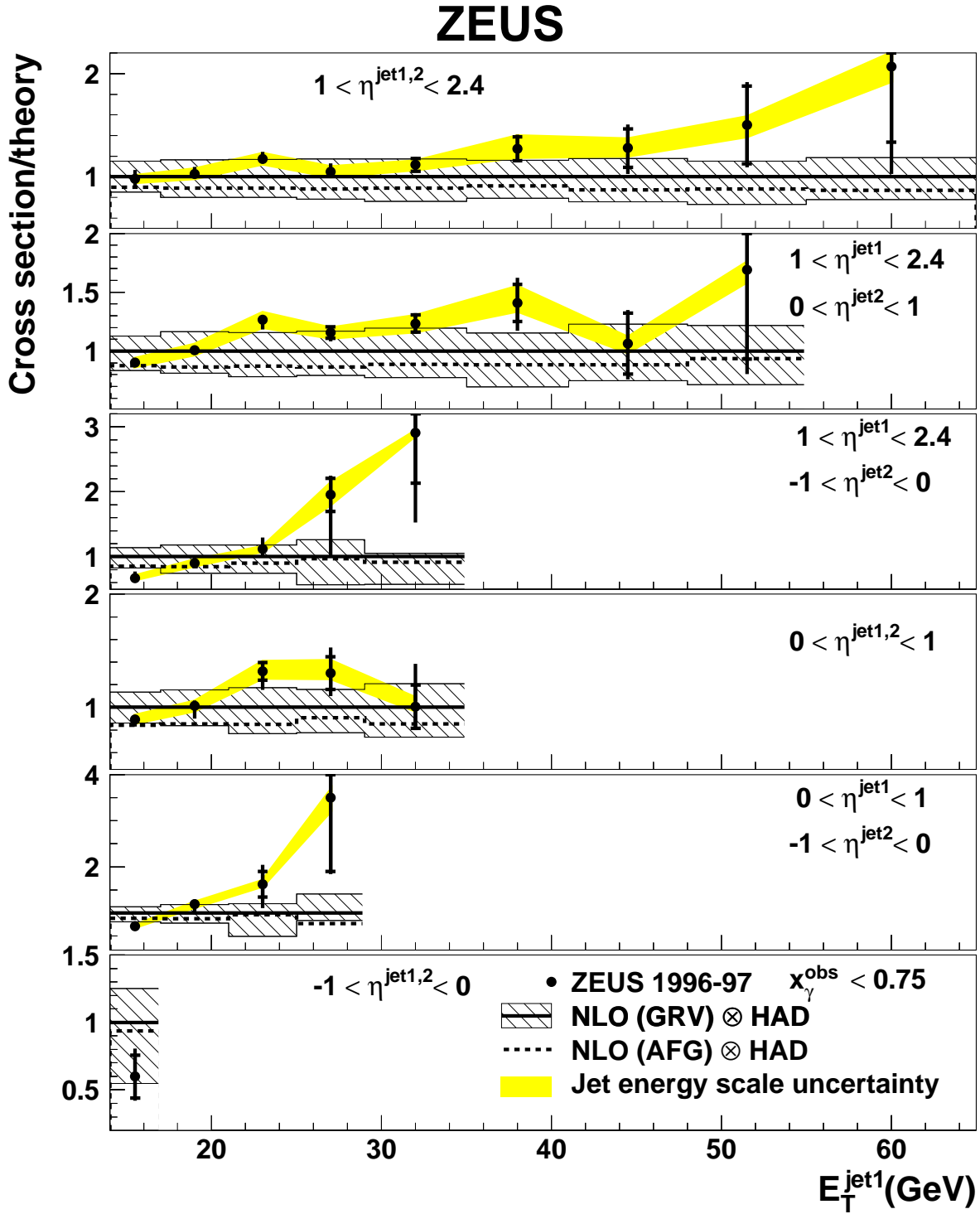


Figure 7: Ratio of cross sections to the central theoretical prediction as a function of E_T^{jet1} for events with $x_\gamma^{\text{obs}} < 0.75$. The measurement is divided into six regions of the pseudorapidities of the jets. For further details, see the caption to Fig. 3.

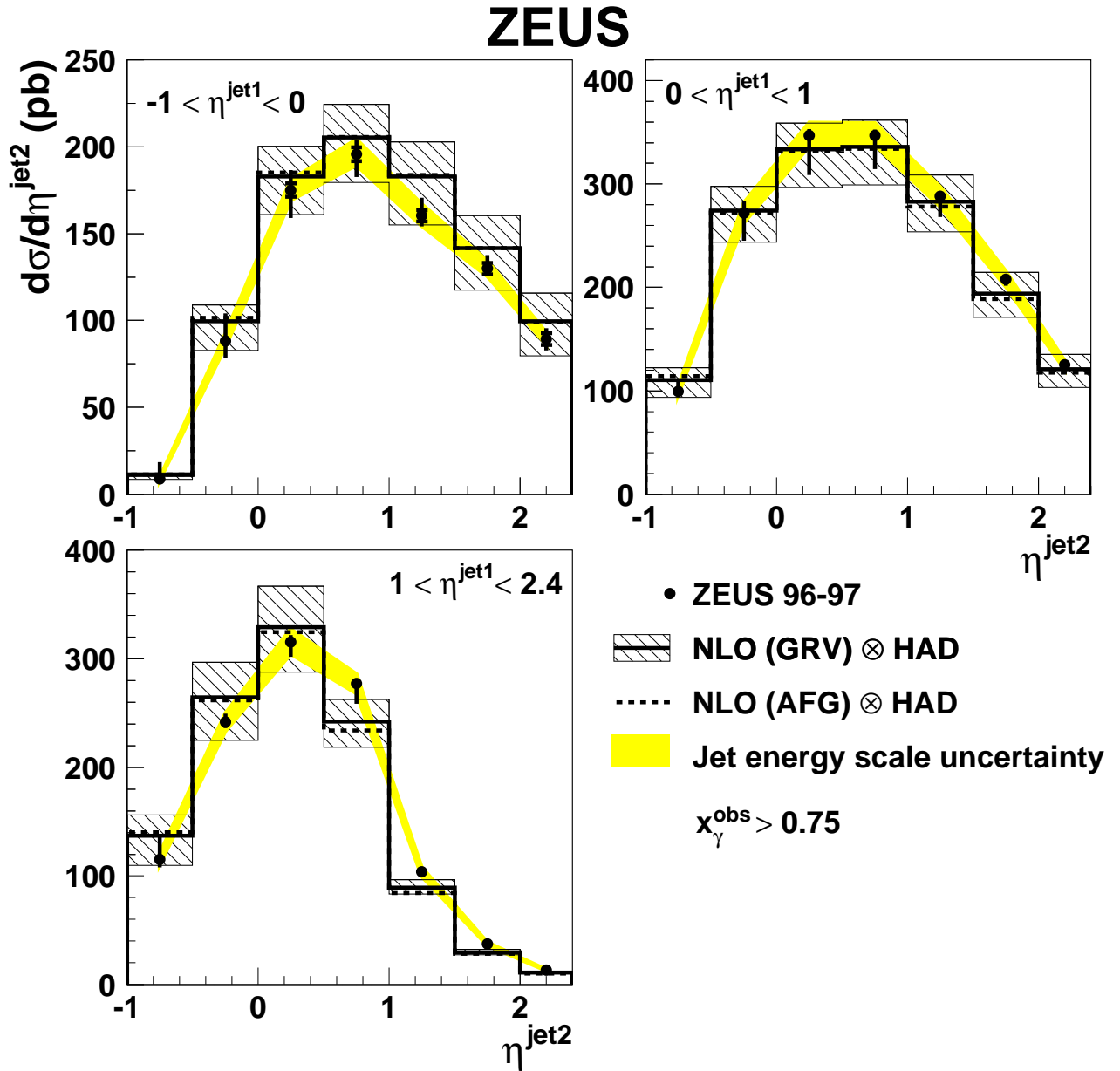


Figure 8: Measured cross section as a function of $\eta^{\text{jet}2}$ for events with $x_\gamma^{\text{obs}} > 0.75$. The measurement is divided into three regions of the pseudorapidity of the other jet. For further details, see the caption to Fig. 3.

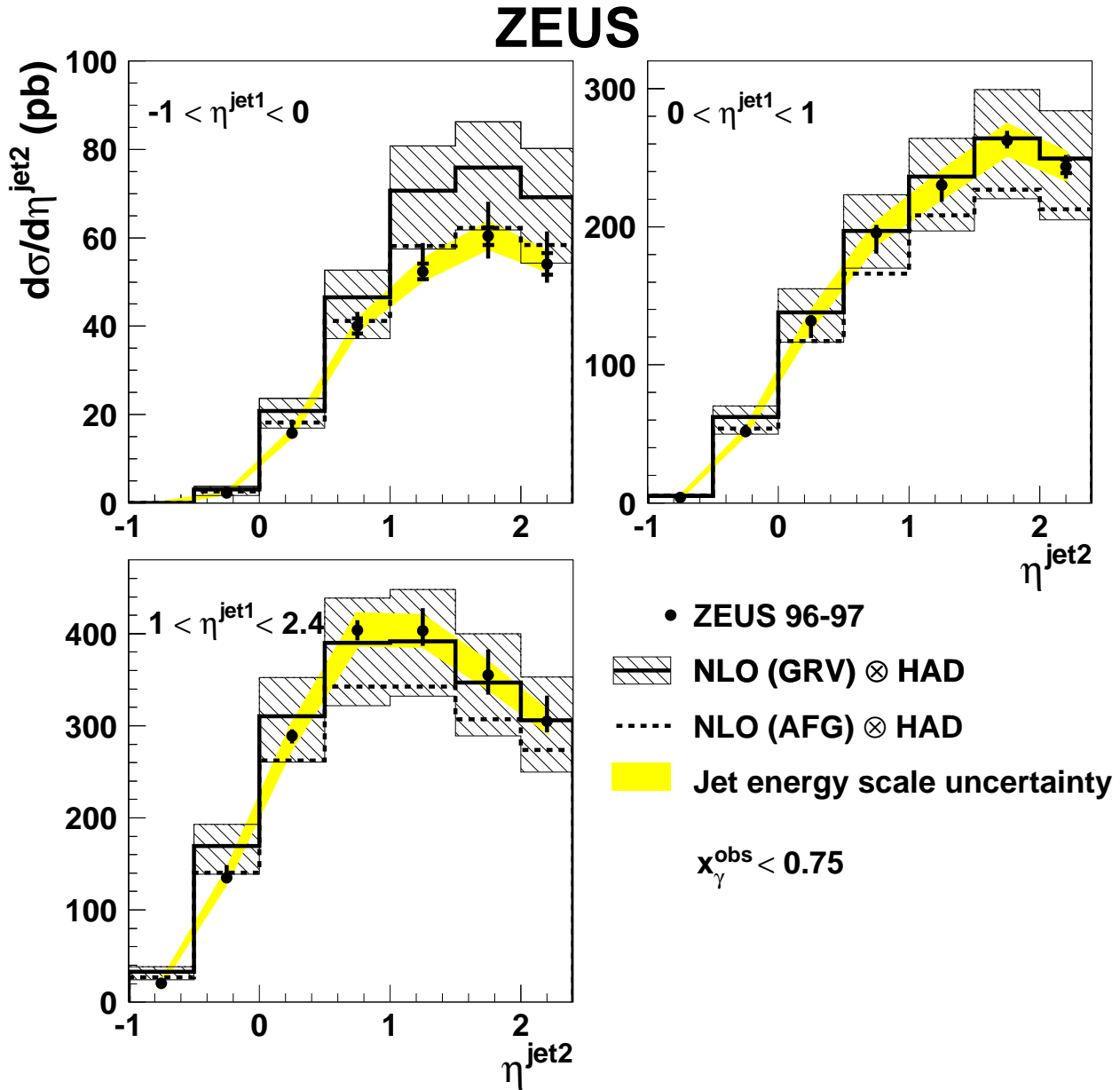


Figure 9: Measured cross section as a function of $\eta^{\text{jet}2}$ for events with $x_\gamma^{\text{obs}} < 0.75$. The measurement is divided into three regions of the pseudorapidity of the other jet. For further details, see the caption to Fig. 3.

ZEUS

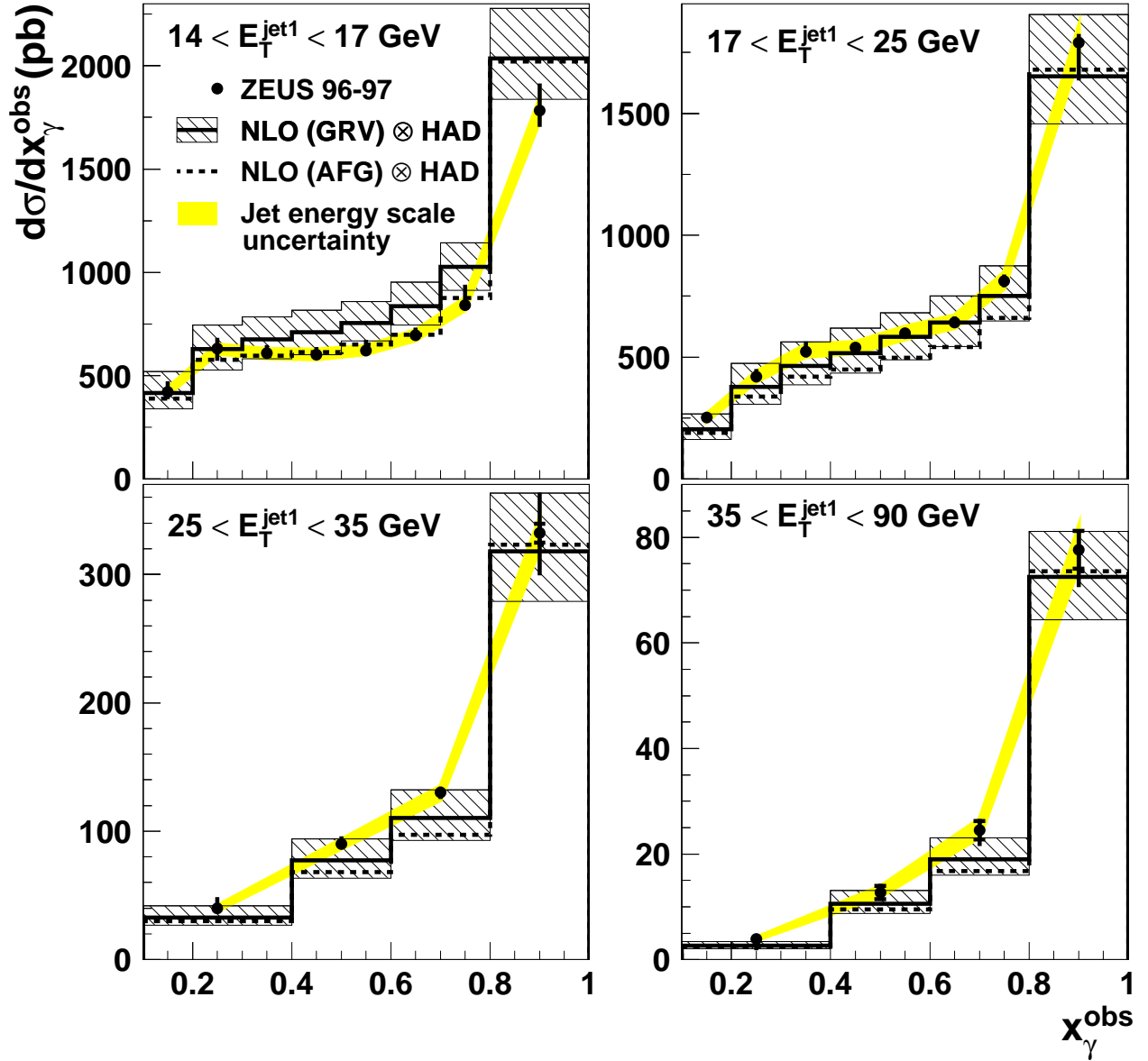


Figure 10: Measured cross section as a function of x_γ^{obs} in four regions of E_T^{jet1} compared to NLO predictions. For further details, see the caption to Fig. 3.

ZEUS

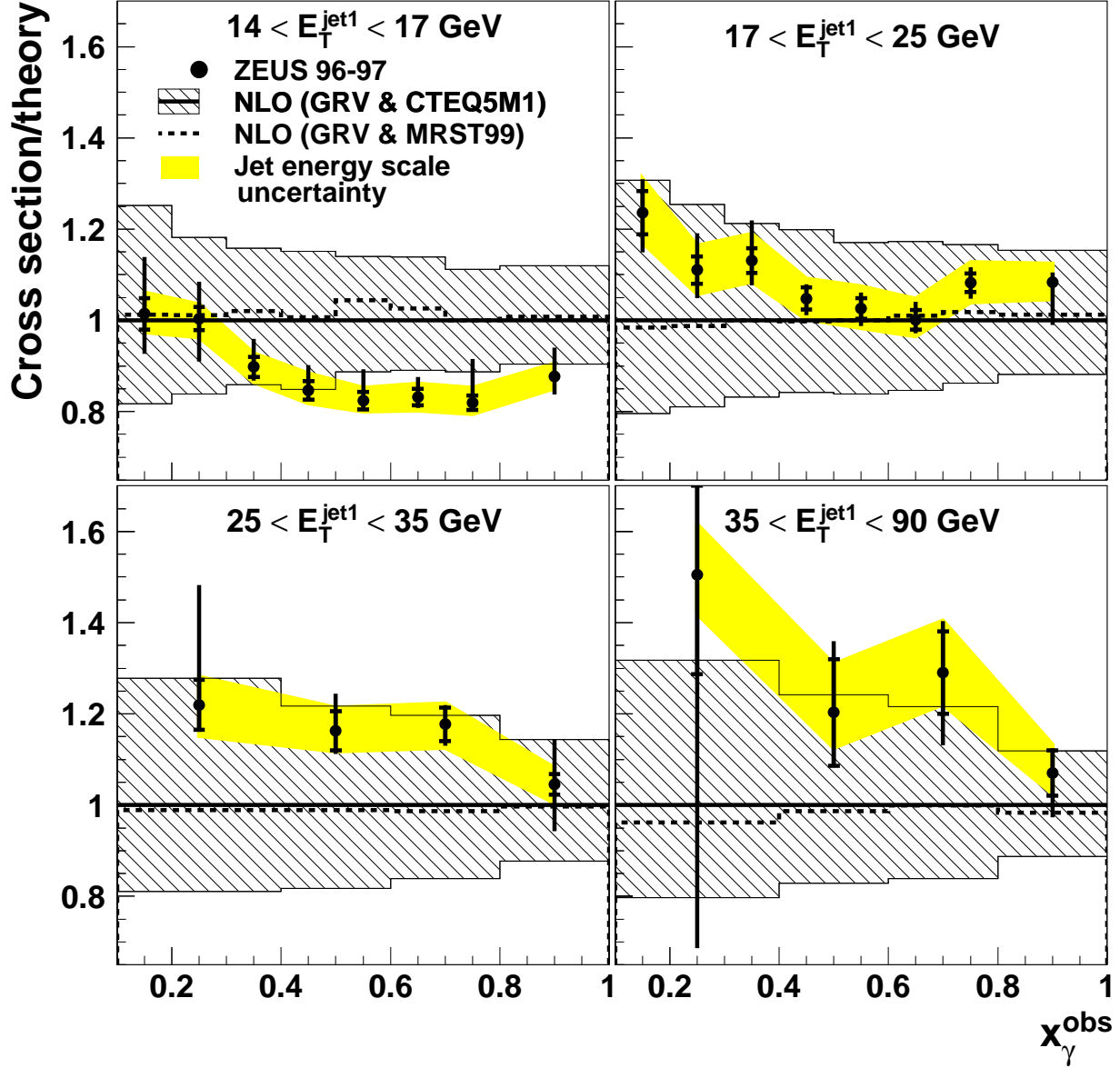


Figure 11: Ratio of cross sections to the NLO prediction using GRV-HO and CTEQ5M1 as the photon and proton PDFs, respectively, and the scale set to $E_T/2$ as a function of x_γ^{obs} in four regions of E_T^{jet1} . The data are shown with statistical errors (inner bars) and statistical and systematic uncertainties added in quadrature (outer bars). The uncertainty due to that of the jet energy scale is shown as the shaded band. The theoretical uncertainty is shown as the hatched band. Predictions using MRST99 (dashed line) for the proton are also shown.

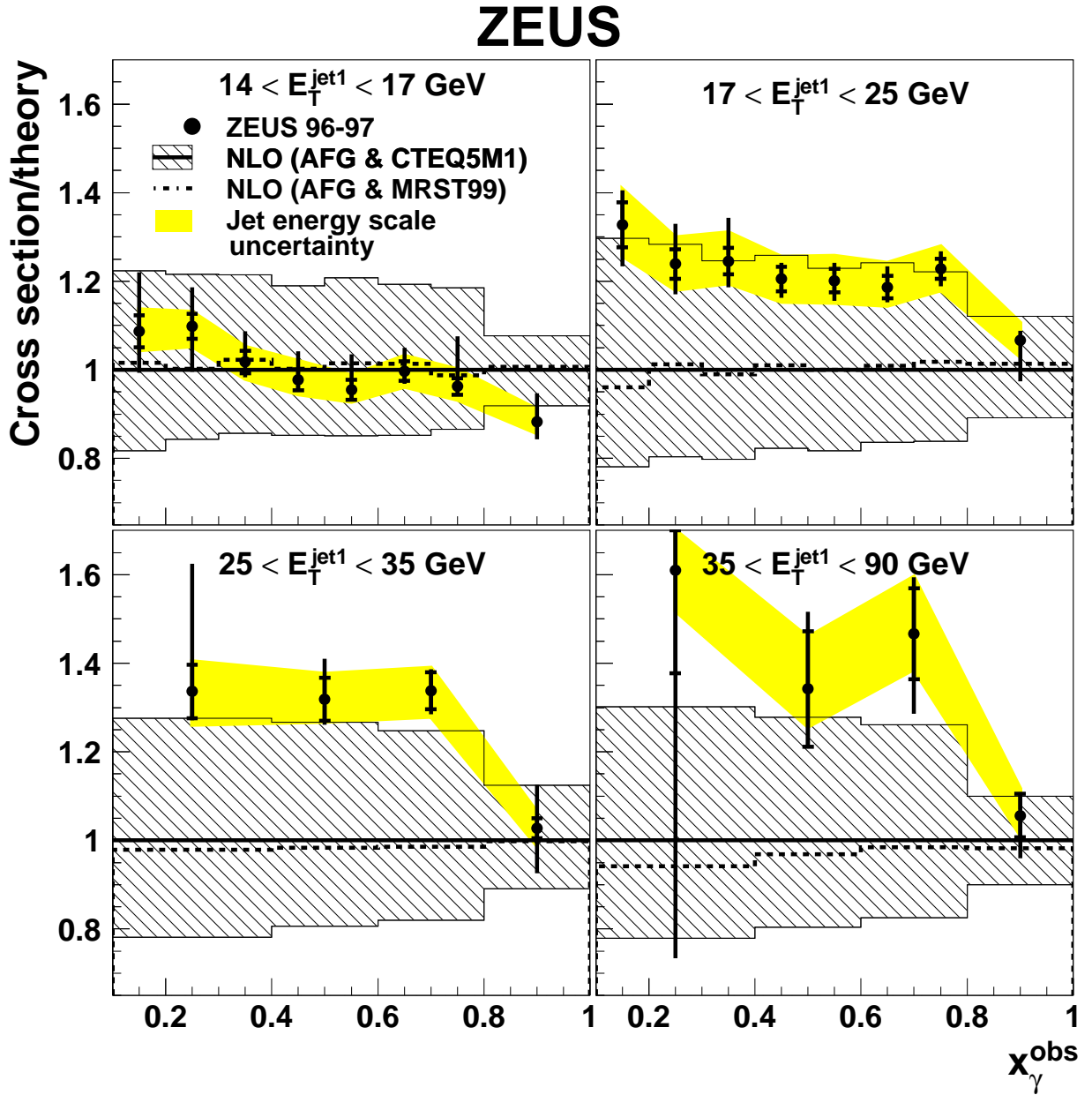


Figure 12: Ratio of cross sections to the NLO prediction using AFG-HO and CTEQ5M1 as the photon and proton PDFs, respectively, and the scale set to $E_T/2$ as a function of x_γ^{obs} in regions of E_T^{jet1} . For further details, see the caption to Fig. 11.

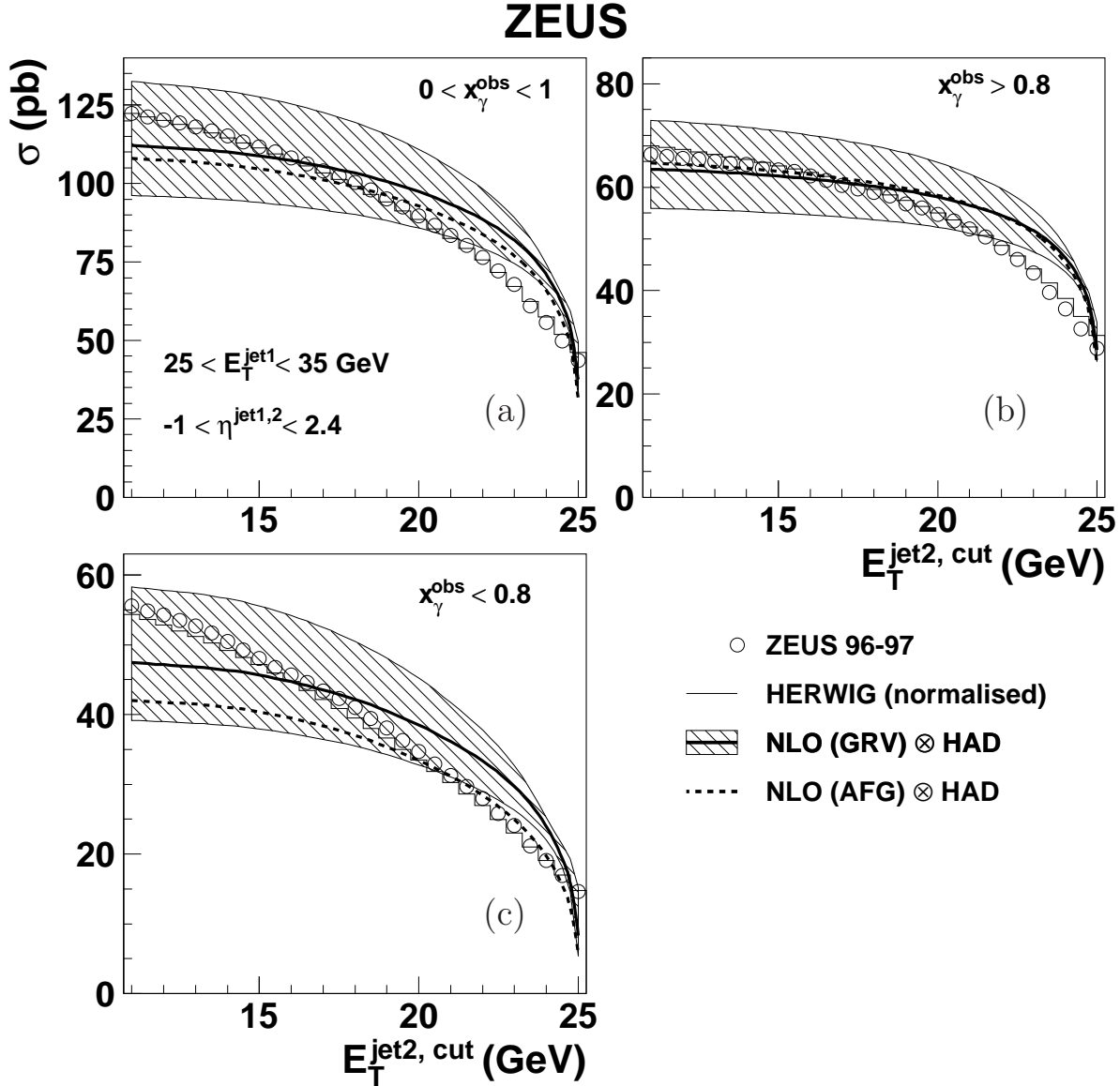


Figure 13: Measured cross section as a function of $E_T^{\text{jet2,cut}}$ for a fixed range of transverse energy of the leading jet, $25 < E_T^{\text{jet1}} < 35 \text{ GeV}$, compared to MC simulation and NLO predictions for (a) $0 < x_\gamma^{\text{obs}} < 1$, (b) $x_\gamma^{\text{obs}} > 0.8$ and (c) $x_\gamma^{\text{obs}} < 0.8$. The typical magnitude of the statistical and systematic uncertainties added in quadrature is $\pm 10\%$. The NLO prediction, corrected for hadronisation effects, calculated using the GRV-HO and CTEQ5M1 PDFs for the photon and proton, respectively, is shown as the thick solid line. The shaded band represents the quadratic sum of the systematic uncertainties, as discussed in Section 10.2. The prediction using the AFG-HO photon PDF is shown as the dashed line. The prediction of HERWIG, calculated using the GRV-LO and CTEQ4L PDFs for the photon and proton, respectively, is normalised to the first point in the range $0 < x_\gamma^{\text{obs}} < 1$; it is shown as the histogram.